Lappeenranta University of Technology
Faculty of Technology
LUT Mechanical Engineering
Degree Program in Mechanical Engineering

Eerik Sikanen

MECHANICAL DESIGN AND ANALYSIS OF MODULAR ACTIVE MAGNETIC BEARING TEST RIG

Examiners: Professor Jussi Sopanen
Dr. Sc. (Tech.) Rafał Piotr Jastrzębski

ABSTRACT

Lappeenranta University of Technology
Faculty of Technology
LUT Mechanical Engineering
Degree Program in Mechanical Engineering

Eerik Sikanen

Mechanical design and analysis of modular active magnetic bearing test rig

Master's Thesis

2014

74 pages, 53 figures, 6 tables and 3 appendices

Examiners: Professor Jussi Sopanen
Dr. Sc. (Tech.) Rafał Piotr Jastrzębski

Keywords: active magnetic bearing, rotor, high speed, electric machine, shrink fit.

In this master's thesis, the mechanical design and analysis of a modular active magnetic bearing (AMB) test rig is investigated. First the theory of high speed rotor design is presented. Also a number of analytical methods for analyzing mechanical stresses of high speed rotor is presented. Due to the nature of high speed machinery, introduction to rotordynamics and analyzing methods is presented. The structure and functionality of AMBs used in this study are introduced. In addition, a literature review of test rigs, used in various applications, such as component identification and rotor dynamics studies, is presented.

The thesis scope was chosen to provide a concept design of a reconfigurable test rig, the design and modelling of a rotor of a high-speed induction motor and a documentation of the design process, with the main focus being on the rotor design. The need of reconfigurable modular design comes from the possibility of changing the system configuration, in order to test and perform the identification of different AMBs, motor and rotor designs. Structures of modular actuator designs for AMBs and electric machine are presented and the benefits of having a modular structure are discussed.

Both analytical and finite element methods are presented and used for analyzing the designed high speed rotor. The results are presented and compared for finding differences between various modeling methods. Finally, the complexity and requirements of mounting the electromagnetic components to the rotor and actuator modules for optimizing both the mechanical and the electromagnetic performance are discussed.

TIIVISTELMÄ

Lappeenrannan teknillinen yliopisto
Teknillinen tiedekunta
LUT Konetekniikka
Konetekniikan koulutusohjelma

Eerik Sikanen

Modulaarisen magneettilaakeroidun koelaitteen mekaaninen suunnittelu ja analysointi

Diplomityö

2014

74 sivua, 53 kuvaa, 6 taulukkoa ja 3 liitettä

Tarkastajat: Professori Jussi Sopanen
TkT Rafał Piotr Jastrzębski

Hakusanat: aktiivimagneettilaakeri, roottori, suurnopeus, sähkökone, kutistussovite.

Tässä työssä on tutkittu modulaarisen aktiivimagneettilaakeroidun koelaitteen mekaanista suunnittelua ja analysointia. Suurnopeusroottorin suunnittelun teoria on esitelty. Lisäksi monia analyyttisiä mallinnusmenetelmiä mekaanisten kuormitusten mallintamiseksi on esitelty. Koska kyseessä on suurnopeussähkökone, roottoridynamiikka ja sen soveltuvuus suunnittelussa on esitelty. Magneettilaakerien rakenteeseen ja toimintaan on tutustuttu osana tätä työtä. Kirjallisuuskatsaus nykyisistä koelaitteista esimerkiksi komponenttien ominaisuuksien tunnistamiseen ja roottoridynamiikan tutkimuksiin on esitelty.

Työn rajauksena on konseptisuunnittelu muunneltavalle magneettilaakeroidulle (AMB) koelaitteelle ja suunnitteluprosessin dokumentointi. Muunneltavuuteen päädyttiin, koska se mahdollistaa erilaisten komponenttiasetteluiden testaamisen erilaisille magneettilaakerikokoonpanoille ja roottoreille. Pääpaino tässä työssä on suurnopeus induktiokoneen roottorin suunnittelussa ja mallintamisessa. Modulaaristen toimilaitteiden kuten magneettilaakerien ja induktiosähkömoottorin rakenne on esitelty ja modulaarisen rakenteen käytettävyyden hyödyistä koelaitekäytössä on dokumentoitu.

Analyyttisiä ja elementtimenetelmään perustuvia tutkimusmenetelmiä on käytetty tutkittaessa suunniteltua suurnopeusroottoria. Suunnittelun ja analysoinnin tulokset on esitelty ja verrattu keskenään eri mallinnusmenetelmien välillä. Lisäksi johtopäätökset sähkömagneettisten osien liittämisen monimutkaisuudesta ja vaatimuksista roottoriin ja toimilaitteisiin sekä mekaanisten että sähkömagneettisten ominaisuuksien optimoimiseksi on dokumentoitu.

PREFACE

I wish to thank my supervisors for this great subject. I also wish to thank the personnel of Machine Design, Machine Dynamics and Laboratory of Control Engineering and Digital Systems of Laboratory of Electrical Engineering with whom I had a great time collaborating. Great thanks also to LUT Voima prototype laboratory which is going to perform a detailed design and will be handling the fabrication of reconfigurable test rig.

Writing this master's thesis has taken lots of days and nights. The major personal achievements writing this thesis and making the test rig designs were new knowledge of high speed machinery possibilities and rotordynamics and also active magnetic bearing technology. In addition, I learned to used powerful finite element software ANSYS. Also, my experience of using MATLAB as numerical tool increased.

Finally, thank you to

Lappeenranta, September 19th 2014

Eerik Sikanen

CONTENTS

ABBREVIATIONS AND SYMBOLS

Abbreviations

AMB	active magnetic bearing
DOF	degrees of freedom
FEA	finite element analysis
FEM	finite element method
IM	induction motor
OD	outer diameter
PID	proportional-integral-derivative
RoBeDyn	Rotor-Bearing Dynamics Toolbox for MATLAB
RoMaDyC	Center for Rotating Machinery Dynamics and Control
SB	safety bearing

Roman symbols

A_g	pole face area
$\boldsymbol{C}$	damping matrix
d	diameter
e_{ub}	unbalance eccentricity
E	elastic modulus
F	force
$\boldsymbol{F}$	external force vector
g	air gap
$\boldsymbol{G}$	gyroscopic matrix
i	current
$\boldsymbol{K}$	stiffness matrix
m_{ub}	unbalance mass
$\boldsymbol{M}$	mass matrix
N	number of coil turns
p	pressure *or* pitch
$\boldsymbol{q}^c$	unbalance vector related to constant speed
$\boldsymbol{q}^{nc}$	unbalance vector related to acceleration
$\boldsymbol{q}$	vector of nodal coordinates
$\boldsymbol{Q}_1$	unbalance force vector related to constant speed
$\boldsymbol{Q}_2$	unbalance force vector related to acceleration
r	radius

t_h	thickness
T	torque
t	time
x	displacement

Greek symbols

α	angle *or* thermal expansion coefficient
δ_r	radial interference
Δt	temperature change
ϵ	correction factor
μ_0	magnetic permeability of free space
μ	friction coefficient
ν	Poisson's ratio
ρ	density
σ	stress
ω	angular velocity
Ω	rotational speed

Sub- and superscripts

0	nominal
avg	average
a	axial
f	interference
i	ith node *or* inner
ls	loosening
m	major
n	number of nodes
o	outer
p	pitch
ref	reference
r	radial
th	thread
tot	total
t	tangential *or* tightening
μ	friction

1 INTRODUCTION

1.1 Background

Active magnetic bearing (AMB) systems are known for their good performance and accuracy in high speed technology because the frictionless magnetic bearings generate the best support in high speed machinery. In order to prevent any damage to AMBs, an additional safety bearing (SB) system is typically installed side by side with the AMB system. In case of failure in the AMB control system, the safety bearings, which are typically ball bearings, will generate the required support to the rotor. Testing of the AMB control systems and safety bearing behavior in a laboratory environment is much safer than with a real system, where high power machinery can cause difficult situations. Fig. 1 presents an example configuration of a laboratory environment AMB test rig [1]. By designing and fabricating a reconfigurable AMB test rig and providing a component identification environment different dynamic phenomena can be achieved in laboratory.

Figure 1. Multipurpose reconfigurable AMB test rig [1]

1.2 Objectives and restrictions

In this master's thesis mechanical design and analysis of reconfigurable test rig is investigated. A reconfigurable concept provides various test configurations with just minor modification. In order to make different laboratory tests, the rotor and AMB actuator module designs need to be reconfigurable. Therefore, the capability of changing key components must be taken into account in the design iteration. A literature review of current AMB-system test rigs is introduced. The concept design and analysis in this thesis covers Configuration I, which is the first of three upcoming design configurations in the Reconfigurable test rig project. Configuration I consist of two radial AMBs, one axial AMB and an induction motor. Its main purpose is to study the accuracy and the functionality of the modular design. Configuration II uses conical AMBs which provide both the radial and the axial support. This configuration consist of thee modules, two conical AMBs and an induction motor module. Configuration III is a bearingless motor, where two radial AMBs and the induction motor are combined into two stators providing both motoring and suspension. This design uses conventional axial AMB support.

1.3 Structure of the thesis

The theory of design and the analysis for a high speed rotor are introduced in section 2. The design and results of the analysis, with the main focus being on the high speed rotor design, are presented in section 3. In addition, the design specifications of Configuration I are introduced in section 3. Section 4 is added in order to present more information about the Reconfigurable test rig project. The section presents two additional test rig configurations and also possible future developments in the project. Discussion of the results is presented in section 5. Since the focus is on one test rig design, section 6 includes conclusions of the design's first configuration. The design parameters, which are fulfilled in the thesis, are presented in Appendix 1. Also, Appendix 3 include figures of the fabricated Configuration I rotor and modules on the base plate and the supporting structure.

1.4 Current AMB test rigs

This section presents a literature review of current AMB and rotor–bearing-research test rigs. Most of the research articles found focus on the AMB control system. Therefore,

the main discoveries are introduced in order to present variety and the importance of laboratory identification.

1.4.1 RoMaDyC test rigs

As an example of an existing test rigs, Center for Rotating Machinery Dynamics and Control (RoMaDyC) has developed several high speed capable test rigs. A general purpose AMB test rig is introduced in Fig. 2. It has five standard magnetic levitation axes and four external excitations, altogether nine magnetically controlled axes. The fully adjustable rotor is driven by an electric motor with a maximum of 15 000 rpm and is connected to the motor with flexible coupling. The diameter of the shaft and position of the unbalance disk can be varied. The AMB test rig is equipped with dSPACE data acquisition unit. By using this unit, a number of experimental prototype controllers can be tested. In addition, the test rig is also equipped with an industrial standard proportional-integral-derivative (PID) controller that can be used for evaluating experimental controllers. [1]

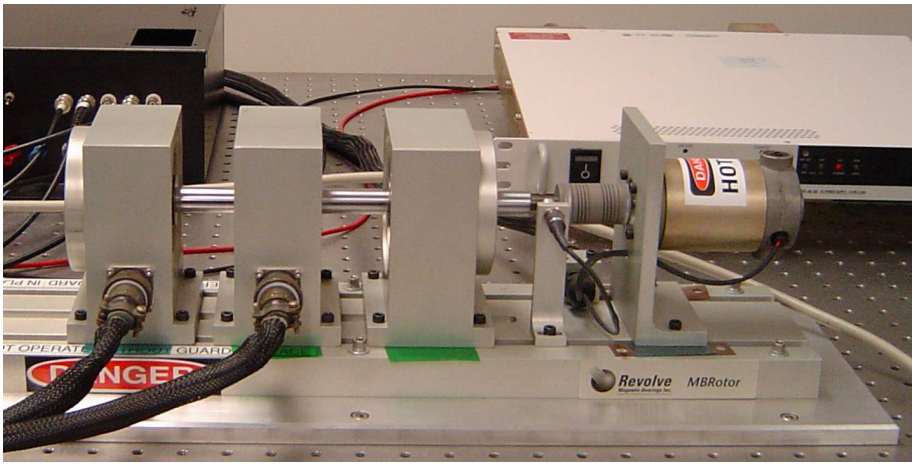

Figure 2. RoMaDyC General Purpose AMB Test Rig [1]

In addition, RoMaDyC has multiple AMB and rotordynamics related test rigs. A Crack Test Rig is constructed for crack detection research for shafts, disks, bearings and couplings. With condition monitoring sensors and data acquisition, the test rig can be used to study cracks, cuts, rubbing, looseness and misalignment. The multipurpose rotordynamic test rig is used for studying classical rotordynamics phenomena, such as unbalance response, gyroscopic effect and alignment issues. Fig. 3 presents a test rig for

fluid film bearings. The test rig is constructed on an optical grade isolation table to protect it from unwanted vibrations. Perpendicularly installed eddy current position sensors are used to measure changes in orbit. [1]

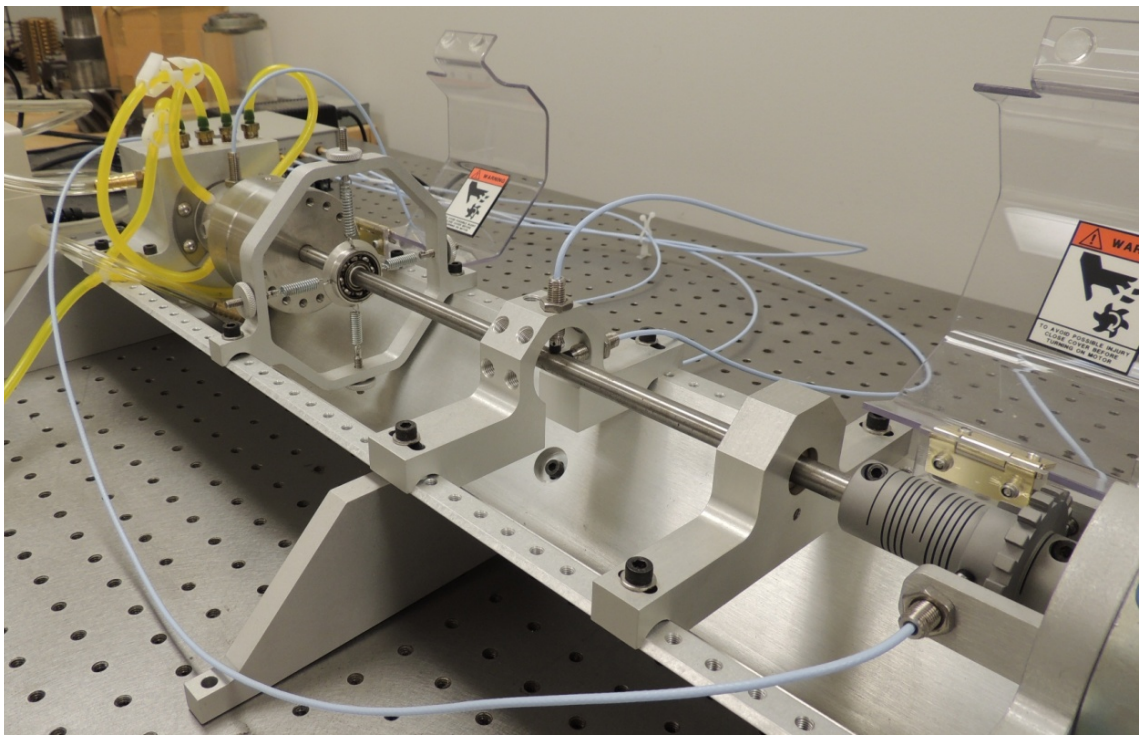

Figure 3. Fluid film bearing test rig [1]

1.4.2 Self Bearing Motor

A research project at the University of Alberta focuses on a self-bearing motor, also known as a bearingless motor, which is a function of an electric motor with a magnetically integrated bearing. This combination includes an single actuator that provides magnetic levitation and rotation simultaneously. The main advantages are increased power density and the reduction of shaft length which also benefits rotordynamic performance. A contactless servomotor motor illustrated in Fig. 4 consists of a permanent magnet synchronous machine with a high torque–to–inertia ratio. Unique features in bearingless servomotors are slotless stator construction and an all-Lorentz operating principle which, yields a simpler design and smoother torque production. [2]

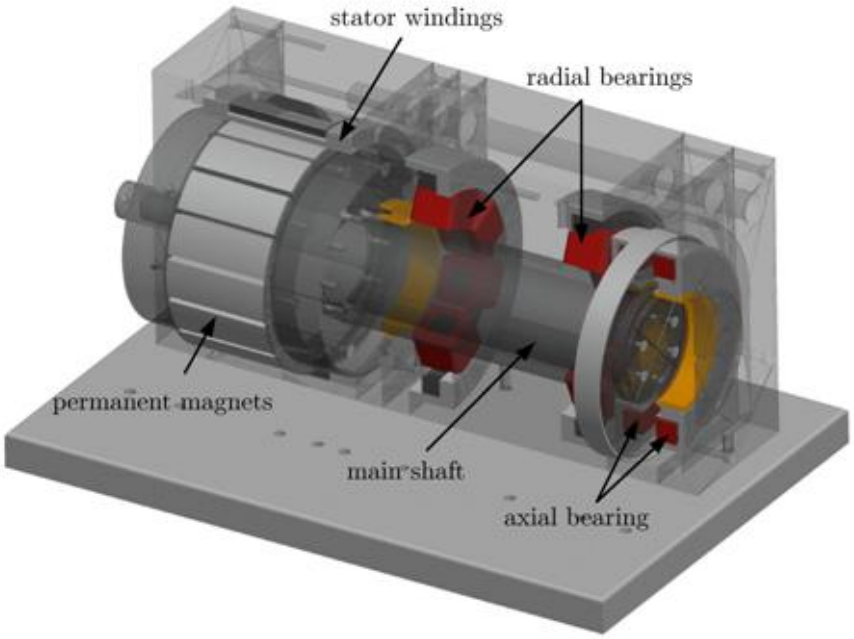

Figure 4. Concept of bearingless motor [2]

1.4.3 Flexible rotor active magnetic bearing test rig

Mushi, Lin and Allaire [3] made a research regarding to the aerodynamic cross-coupled stiffness forces and uncertain loads of the stability of AMB supported turbomachinery. In order to excite disturbance in the AMBs, an exciter is added to the rotor to emulate an impeller and a high pressure oil seal. Due to the limitation of the test cell's foundation, the rotor length was limited to 1.23 m, and a belt-drive system was used at maximum operational speed of 15 000 rpm. The test rig and control system are presented in Fig. 5, where the major components are (A) rotor, (B1, B2) exciter discs, (C1) AMB supporting the nondriven end , (C2) AMB supporting driven-end , (D1) AMB for mid-span disturbance, (D2) quarter-span disturbance AMB, (E) motor, (F) amplifier and signal conditioning rack, and (G) control workstation. [3]

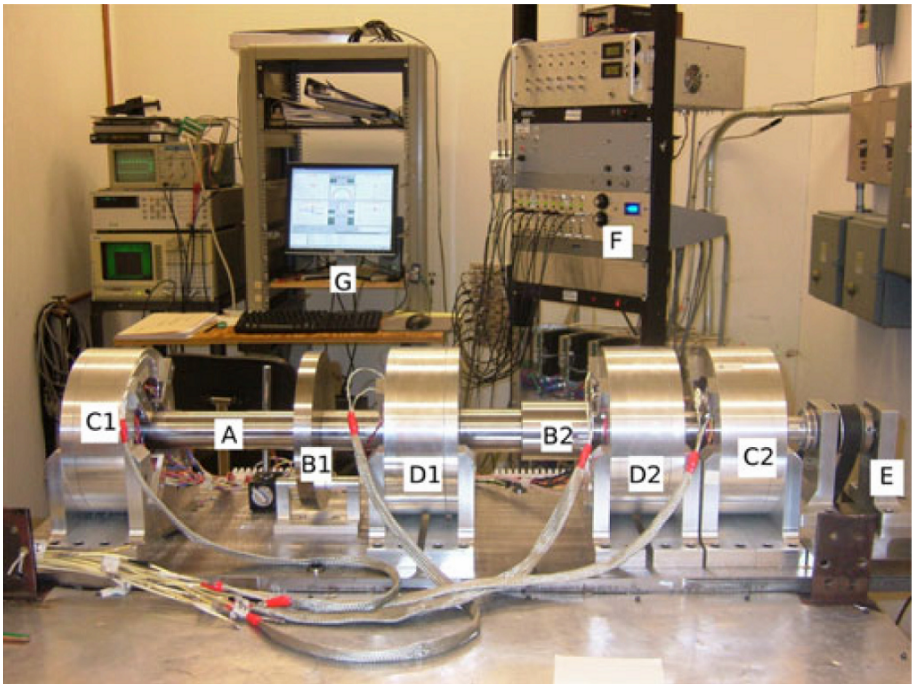

Figure 5. Test rig and control system [3]

2 THEORY OF DESIGN AND ANALYSIS

The main aspect of designing and analysing high speed machinery is introduced in this section. From a mechanical point of view, designing a rotor construction for high speed induction motor (IM) is one of the most demanding tasks possible. Combining both electrical requirements and mechanical durability requires multiple design iterations. The tools used in the design iteration process are for mechanical 3D design SolidWorks® 2013 SP2.0, for strength calculations using finite element method (FEM) ANSYS® Workbench Release 15.0, for numerical modelling MATLAB® R2012b and for producing vector quality figures Inkscape 0.48.

2.1 Overview of design process

Designing an AMB-controlled high speed machine is typically an iterative process. The process begins by defining drive specifications. The next step is the conceptual design which includes a selection of machine and bearing topology used to make a conceptual layout of the system. Preliminary design includes rough dimensioning for the machine and a selection of both mechanical and electrical parameters for the bearings. Then, preliminary material selection, maximum outer dimension calculation and required shrink fits for the shaft and magnetic components for the rotor are conducted. A detail design of mechanical components includes material selections and the final interference calculations. In addition, detailed stress and rotor dynamics analyses are done. Fig. 6 illustrates the steps for an iterative design process. [4] The areas studied in this thesis are the mechanical aspects of conceptual and preliminary design, as well as some parts of detailed design.

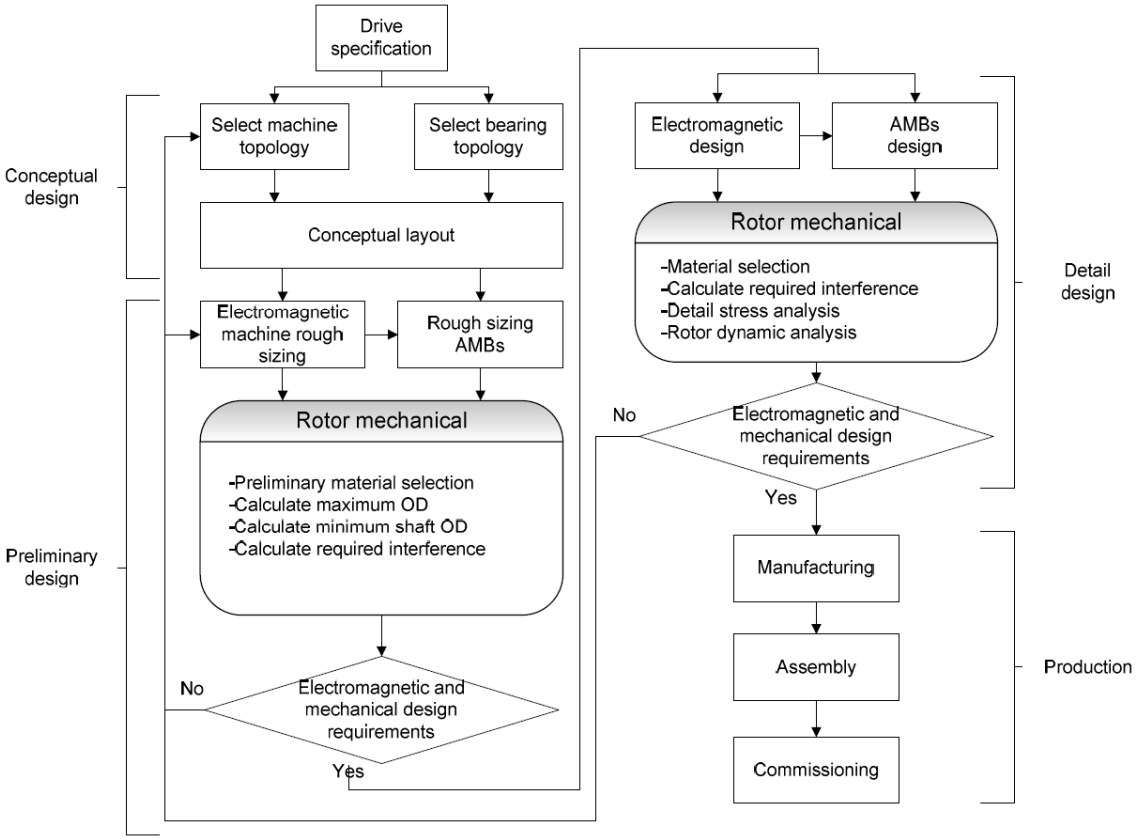

Figure 6. Schematic of iterative design process [4]

Specifications to the system are done in order to define the limits of the machine, such as determining the type of electric motor, dimensions of the rotor, operational speed range and AMB parameters. In the conceptual design phase, the initial layout of the system, positions of the AMBs and motor and of course safety bearing system is defined. In the preliminary design phase of the rotor, the outer diameter (OD) of the rotor is determined in order to ensure its proper functionality within the limits of operational speed. In addition, the required interferences for laminations are initially determined by using analytical equations. The verification of the results is done by finite element analysis (FEA). [4]

Making a detailed design requires dense collaboration in order to match mechanical and electrical requirements. Detailed dimensions and interferences for AMB laminations are determined and a final finite element model of the rotor is performed to verify mechanical performance. [4]

2.2 Introduction to an AMB-supported system

Active magnetic bearings are widely used in high speed machinery. Their contactless performance gives an advantage compared to mechanical ball or rolling element bearings. Because of the high power density AMBs are being used in direct-drive generators and turbomachines. Although AMBs are very reliable, AMB units are typically equipped with safety bearings. The safety bearings generates mechanical bearing support in case of a power surge or additional failure of the AMB controlling system. Safety bearings need to be able to support the rotor in high speed situations while the rotor decelerates. [5, 6]

A rotor drop down may occur in the case of any system failure, such as unpredicted rotor unbalance or any other external disturbance. At this moment, the control of AMBs is closed, causing the rotor to drop on safety bearings. Without safety bearings, the rotor would damage the AMB stator laminations. In general, the air gap of the safety bearing is half of the AMB's air gap. Fig 7 shows the principle layout of AMB-supported rotor with sensors and safety bearings. [5]

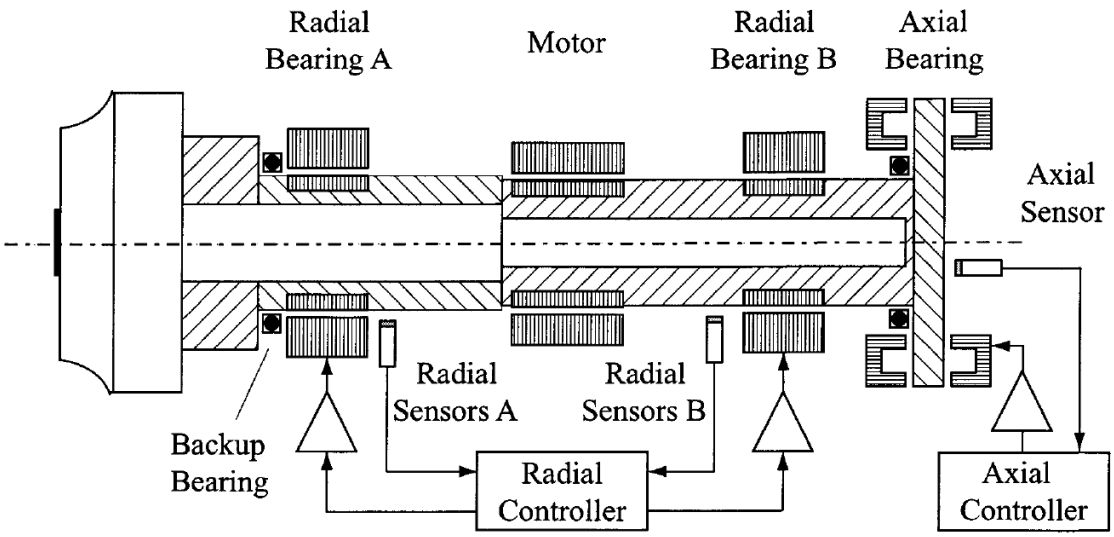

Figure 7. Principle layout of AMB supported rotor with safety bearings [7]

2.3 Active magnetic bearings

AMBs generate contactless bearing support for rotating machinery. This means that the rotor is floating in the air gap and the machine itself operates with only minor air friction losses. Typically, electromagnets in the AMB unit are installed in pairs at opposite sides

of the rotor as seen in Fig. 8. This way, the attractive magnetic forces can be balanced in the electromagnetic actuators and therefore center the rotating element in the control axis. In addition, non-frictional AMBs can operate without any lubrication of the bearing components, therefore allowing the bearing to operate cleanly and virtually maintenance free for long periods of time. Most typically, AMBs are used in turbo compressors because of their high speed capability, minor air friction losses and no need for gear drives and lubrications, making them environmentally friendly. [8]

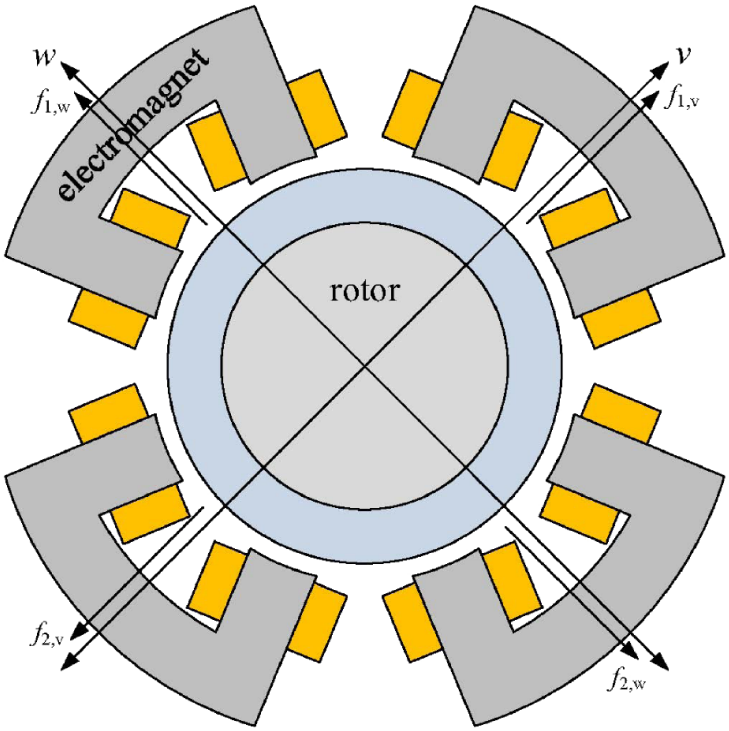

Figure 8. Segmented eight pole radial active magnetic bearing [6]

In order to design a radial AMB unit a number of design specifications need to be taken into account. Electromagnetic performance and therefore the generated force need to be enough to ensure rotor control capability in a normal operational state and also to make possible to accelerate the rotor over possible resonance frequency. A compromise is needed when defining the air gap of an AMB unit. On the other hand, the air gap should be as small as possible; however, some clearance is required in order to ensure possible vibrations of the rotor and also some gap for safety bearings is required.

Additional phenomena to take into account when designing the AMBs are for example the heat dissipation of the coils and possible magnetic eddy current losses in the boundary

surface of the AMB laminations and supporting frame.

2.3.1 Radial AMB structure

The radial AMB stator core is made of electrically optimized thin magnetic metal sheets called laminations. This lamination structure optimizes the flux flow in one direction and minimises eddy current losses in the structure. To optimize rotor levitation, laminations are also attached to the rotor, which are analogically called rotor laminations. Without rotor laminations, eddy current losses would be very high causing the rotor overheat. [5]

Two different AMB pole configurations are presented in Fig. 9. A heteropolar structure presented in Fig. 9a is preferred. In addition, a variation called "E"-core is also one type of heteropolar structure. The "E"-core structure has one center pole, for example a north pole, and two side poles, in this case south poles. A slightly different structure is presented in Fig. 9b, which is the homopolar structure. In this structure, the north and south pole pair is attached axially with respect to the rotor. [5]

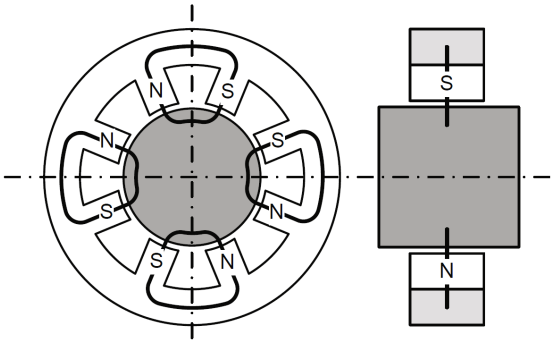

Figure 9. Different types of polarities of AMBs (a) a heteropolar structure and (b) a homopolar structure [5]

2.3.2 Axial AMB structure

In AMB systems, an axial AMB or also known as a thrust AMB, is used to generate support in the axial direction. Fig. 10 presents the structure of an axial AMB. In this case, north and south poles are circular areas of the stator halves of the bearing unit. Therefore, the radial thickness of inner and outer pole surfaces need to be varied so that both pole surfaces saturate at approximately the same coil current as seen in Fig. 10. [5]

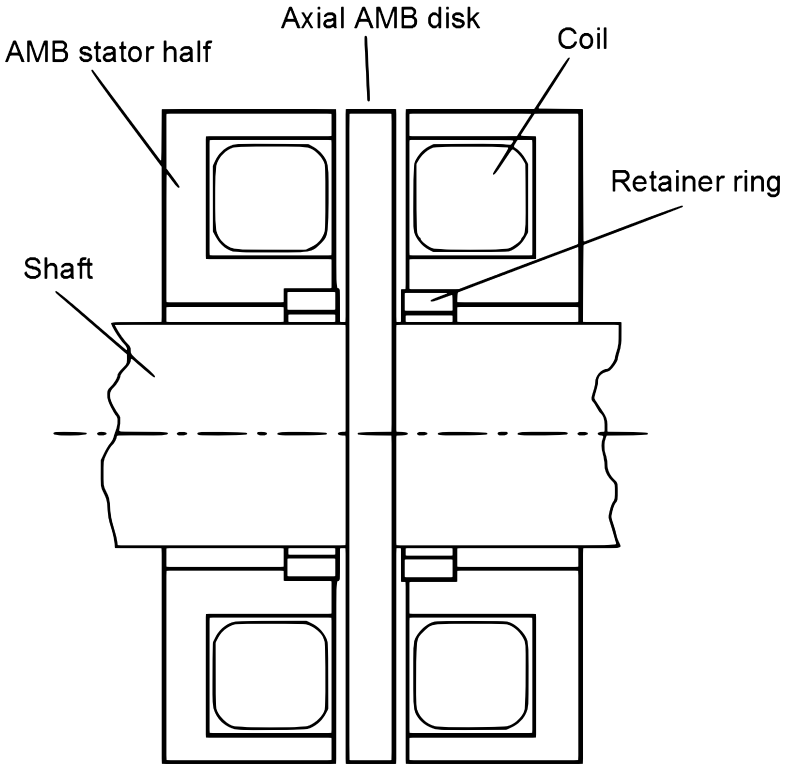

Figure 10. Principle of axial AMB stators and axial disk [5]

On the rotor an axial disk or a thrust disk is placed in order to enable axial control of the rotor. Considering the relatively high diameter of the disk with respect to the diameter of the rotor and centrifugal stresses effecting on the disk in high speed situations, in practice it is very difficult to manufacture a laminated structure for an axial AMB disk. Therefore, the axial disk is made of solid magnetic steel. Typically axial AMB stator halves are also made of solid magnetic steel. Of course electromagnetic performance of a solid stator structure suffers because there is no lamination structure that could disturb the eddy current loops. Yoon [8] proposed one possible method to reduce the eddy current losses by sectioning the stator into eight segments as shown in Fig. 11. This method breaks the

eddy current loop into smaller local loops in each segment of the stator. Brass retainer rings can be used as mechanical bearings in the axial direction. These rings can be press fitted onto AMB stator halves as seen in Fig. 10. As in the case of radial AMBs, the air gaps need to be determined in order to exclude the possibility of the rotor damaging the axial AMB stators or the axial disk. [8]

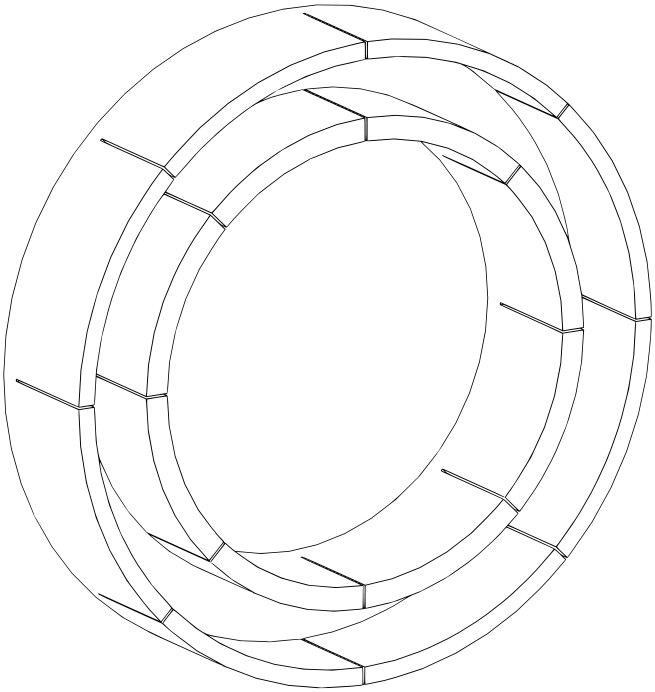

Figure 11. Segmented axial AMB stator

2.3.3 Magnetic force generated by AMB

Since active magnetic bearings operate using a magnetic field produced by passing electric current through a coil, the air gap has a major impact on the magnitude of the magnetic force. In general, if the current is constant, the maximum magnetic force can be generated using the minimum air gap. This approximation is true, if the permeability of iron and possible magnetic saturation effects is neglected. In practice, air gaps used in AMBs are from less than 100 μm to 1 mm depending on the rotor diameter and weight and increasing the air gap decreases magnetic force exponentially. A simple double-sided magnetic actuator is introduced in Fig. 12. The principle of having double-sided AMB poles is to balance the rotor to its nominal position.

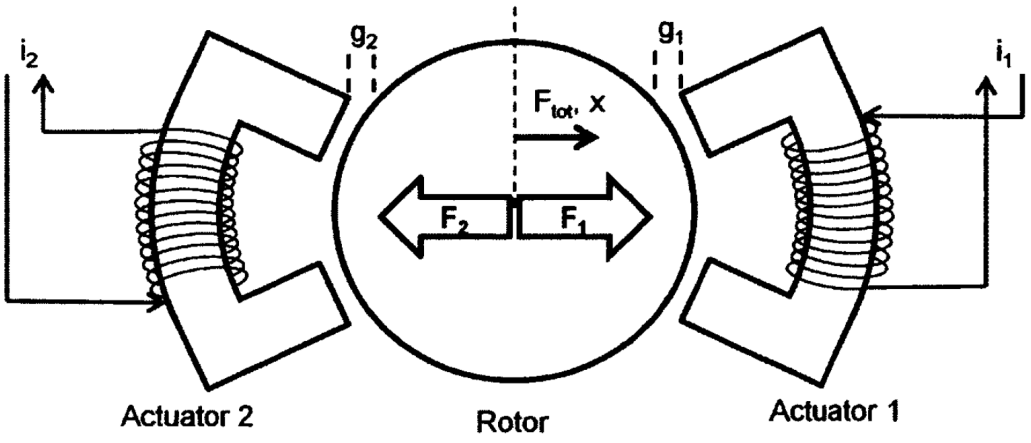

Figure 12. Layout of double sided magnetic actuator [8]

According to Fig. 12, the air gaps g_1 and g_2 can be calculated as follows [8]:

$$g_1 = g_0 - x \tag{1}$$

$$g_2 = g_0 + x \tag{2}$$

where g_0 is the nominal air gap, g_1 is the air gap of actuator 1 as seen in Fig. 12, g_2 is the air gap of actuator 2 and x is the rotor displacement. The nominal air gap g_0 applies on both sides when the rotor is at its nominal position. The linearized force for a double sided-magnetic actuator can be calculated as follows [8]:

$$F_{tot} = \epsilon \mu_0 N^2 A_g \left(\frac{i_1^2}{2g_1^2} - \frac{i_2^2}{2g_2^2} \right) \tag{3}$$

where F_{tot} is the total force, ϵ is the correction factor, μ_0 is the magnetic permeability of free space, N is the number of coil turns, A_g is the pole face area, i_1 and i_2 are the currents of actuators 1 and 2 according to Fig. 12 and g_1 and g_2 are the air gaps of actuators 1 and 2. The correction factor ϵ is for taking the effects of fringing and leakage in the flux path into account, generally $\epsilon \approx 0.8$ for radial AMBs and $\epsilon \approx 0.9$ for axial bearings. [8]

2.3.4 AMB Control system

By their name, AMBs are actively controlled magnetic bearings. In practice, the force of the bearing is actively controlled by electromagnets using a suitable feedback control loop. The main objective of the controller is to maintain the rotor position at its desired value. Position sensors and power amplifiers are essential elements for a control system. A basic control loop is introduced in Fig. 13. In literature, a combination of a power amplifier and an electromagnet of the bearing unit is also called the electromagnetic actuator. [5]

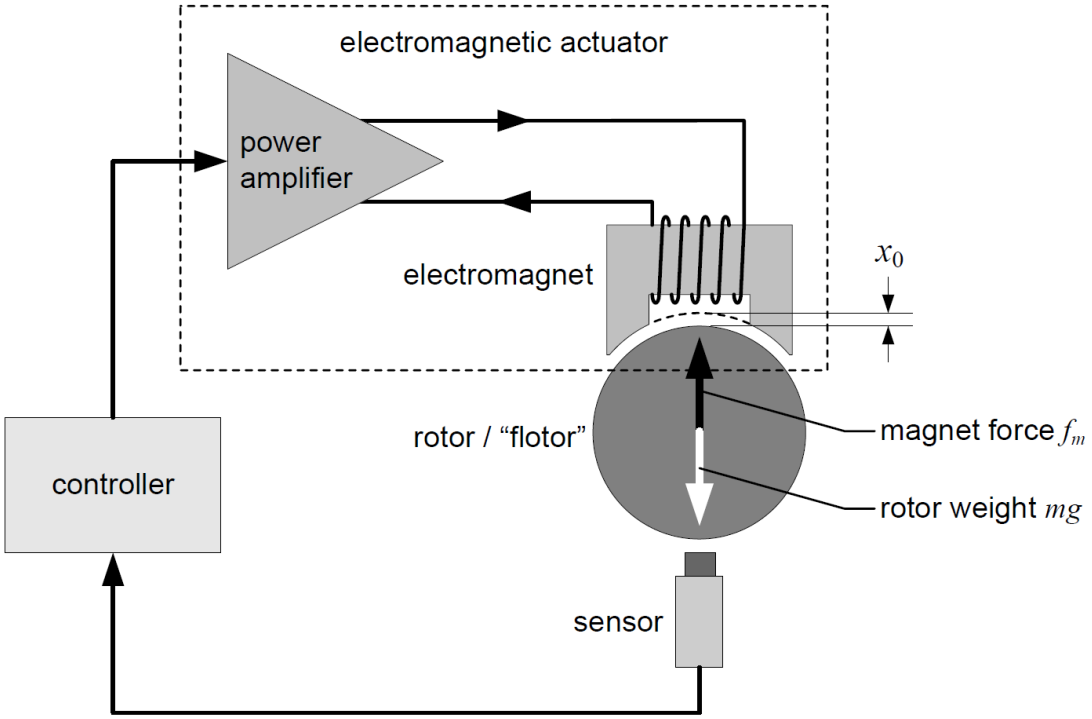

Figure 13. Principle of active magnetic bearing controlling system [5]

Typically adjustable bearing parameters and capabilities of AMBs are static and dynamic stiffness, damping, load-independent static positioning and unbalance force attenuation in rotating systems. A contactless position sensor is typically an eddy current sensor or an inductive type sensor. The sensor steadily measures the deviation between the desired position x_0 as seen in Fig. 13 and the actual rotor position. The controller sends this information to the power amplifier, which operates the electromagnets. [5]

2.4 Safety bearings

2.4.1 Different types of safety bearings

There are two basic types of safety bearings: retainer rings and special ball bearings of which the latter are more common in industrial usage. Active magnetic bearings are used in high speed industrial solutions due to their advantageous properties, such as a very low friction coefficient and the possibility for accurate position control. Still, there are situations when safety bearings are required. If, for some reason, a power failure occurs in an AMB control system, the rotor drops onto safety bearings. In normal system operation with AMBs a very small clearance, called an air gap, is generated between the shaft and safety bearing. Still, in a touch-down situation there is a minor clearance between AMB laminations and the shaft. The air gap for safety bearings is typically half of the air gap of AMBs. Fig 14 illustrates how safety bearings are mounted with AMBs. [5]

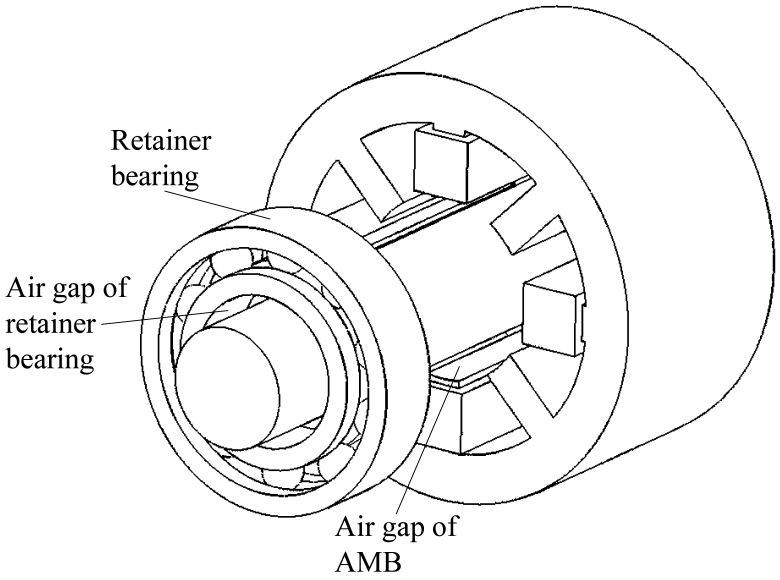

Figure 14. Schematic of safety bearing alongside with AMB [9]

An interesting safety bearing configuration is shown in Fig. 15. Typically, in this kind of configuration the bearings used are angular contact ball bearings installed in x-arrangement. By attaching two radial angular contact bearing on the other end of the rotor, both radial and axial supporting can be enabled.

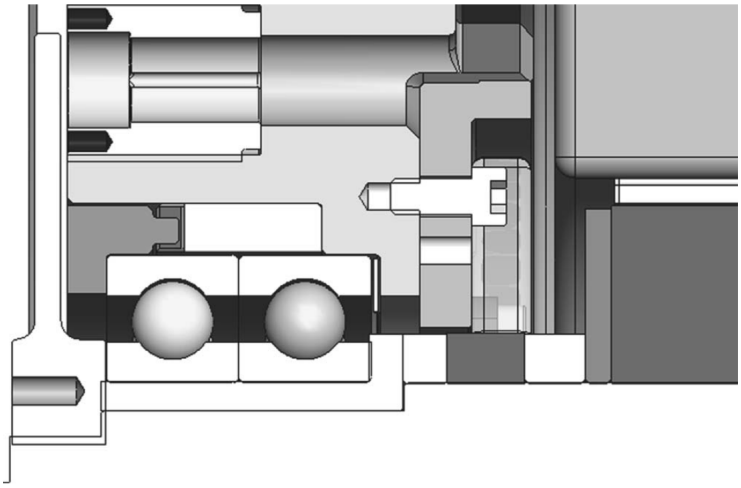

Figure 15. A safety bearing pair providing both radial and axial support [10]

2.4.2 Phenomena in touch-down situation

In the case of emergency situations in general, the rotor does not just drop onto the safety bearings. There are usually a number of different types of motions because of the changing clearance between the shaft and the safety bearing. Three common states of motion in touch-down are: the rotor begins to oscillate, the rotor begins to jump chaotically or there may be a backward whirl motion between the rotor and inner ring of the bearing. The backward whirl motion is the worst kind of motion. If a rotor is unbalanced enough, there may be also fourth state of motion, the forward whirl. All four states of motion are shown in Fig. 16. When the rotor contacts auxiliary bearings, remarkable forces can arise. Those forces can cause high thermal stresses by high slip or rubbing. [5, 11]

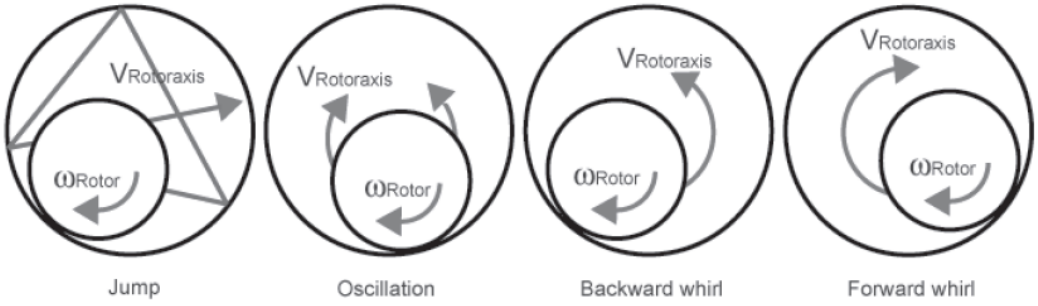

Figure 16. Four different states of motion in touch-down [5]

2.4.3 Requirements for safety bearings

There are design considerations that can prolong the lifetime of a rotor and a safety bearing. The low friction of safety bearing is essential. For avoiding early wearing of the surface of the landing sleeve high strength material with low friction and great hardness should be used. Also, the cleanliness of the safety bearing increases its lifespan. Special damping components have been designed to reduce the high initial impact forces in a touch-down situation, such as damping ribbons which are inserted between the outer ring on the safety bearing and the bearing housing. Fig. 17 presents an O-ring made of elastomer and Fig. 18 presents an elastic tolerance ring. The damping elements with high damping and low stiffness can be useful to avoid critical behavior. This kind of elastically soft support can limit the whirl frequency and amplitude. However, in order to maintain the alignment of the support structure, it should be sufficiently rigid. [5]

Ball bearings are the most common kind of safety bearings. Ball bearings with coated or ceramic balls have good results in reducing the inertia of the bearing ring. Safety bearings in a heavy load environment may last only a few touch-downs. The time for permanent contact has to be kept short to avoid overheating. At the same time, the rotor should be actively slowed down. The internal clearance of bearing has to be enough to allow thermal expansion. [5]

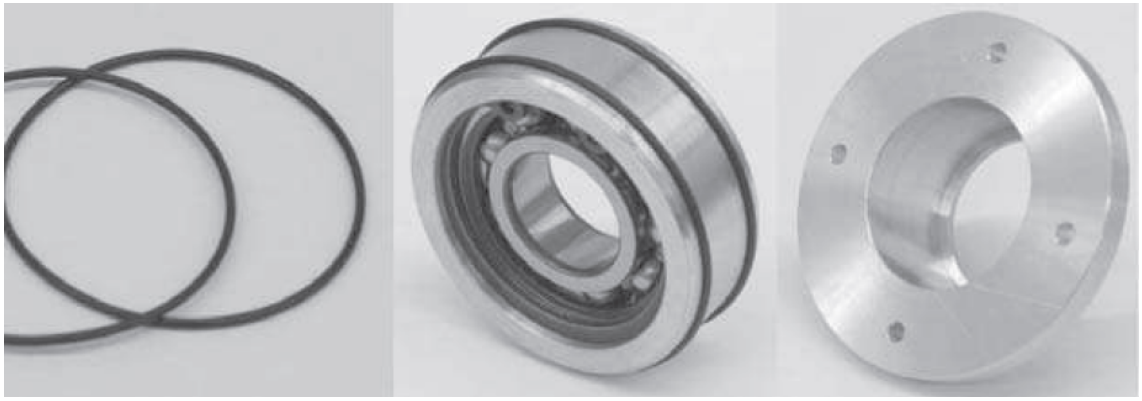

Figure 17. O-ring damping element made of elastomer [5]

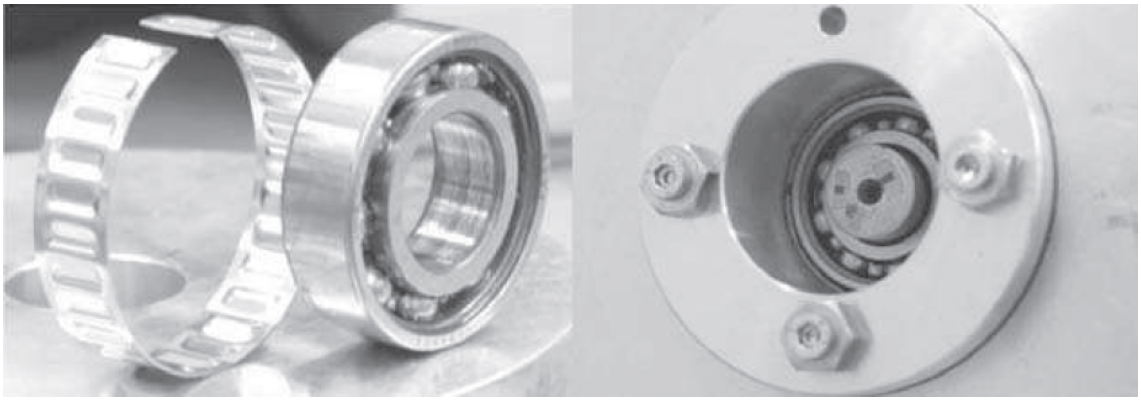

Figure 18. Elastic tolerance ring [5]

According to the article by Swanson *et al.* [6], there are three basic issues that need to be taken into account according to the auxiliary bearing system design perspective. The auxiliary bearing system should prevent all stator-rotor contacts during all operational phases. In a standby state, the bearing needs to remain functional for its life, meaning it needs to withstand corrosion, vibration and heat. An auxiliary bearing needs to have an adequate operational life. [6]

The are other main issues concerning the bearing mounting. When the rotor drops to the auxiliary bearings, the contact creates forces which cause vibration to the support. If the vibration exceeds the limit the bearing mounting frame can yield, the mounting can hit a hard stop and stiffness can suddenly increase and therefore damping can decrease. This can be typical in the case of a violent backward whirl. In the case of complex mounting features, such as friction interfaces, it is difficult to predict how the mounting will respond without experimental data of a particular system. [6]

The response of an auxiliary bearing system is very nonlinear. The radial stiffness of the auxiliary bearing assembly must be sufficient to withstand a sudden shock load and be equal to the full capacity of the magnetic bearing. The auxiliary bearing needs to be designed to survive at least two delevitations from maximum speed to zero with normal aerodynamic breaking. The most common safety bearings are dual full complement angular contact ball bearings. In the case of planetary auxiliary bearing, the DN value of the bearing may become a concern especially with large diameter and in high speed applications due to the construction of this particular bearing design. [6, 12]

Some additional requirements exist for other types of safety bearings. Plain sleeve bearings can be used as safety bearings. They are typically made of bronze, Babbitt

or graphalloy material. Bronze is the most suitable material for heavier shafts and higher speeds. Soft material reduces the risk of damaging or scoring the shaft during a drop. On the other hand, graphalloy generates a lower friction coefficient than bronze and it is suitable for higher temperatures. [12]

2.5 Analytical equations for shaft and sleeve contact

The high speed rotor that is reviewed in this thesis contains multiple separate parts, which are assembled to the rotor using either interference fits or threads. Therefore, in this section a number of analytical equations that can be used to determine proper interference fits and thread tightening torques are presented. These equations are used in the design iteration process of the test rig Configuration I rotor.

2.5.1 Calculating interference fit and pressure

Shrink fit is an interference fit which is caused by heating or cooling the sleeve part. The principle of interference fit is presented in Fig. 19. The following equation describes how the radial shrink fit can be calculated [13]:

$$\delta_r = \alpha r_f \Delta t \tag{4}$$

where δ_r is the radial interference, α is the linear thermal expansion coefficient of a specific material, r_f is the inner radius of sleeve and Δt is the temperature change.

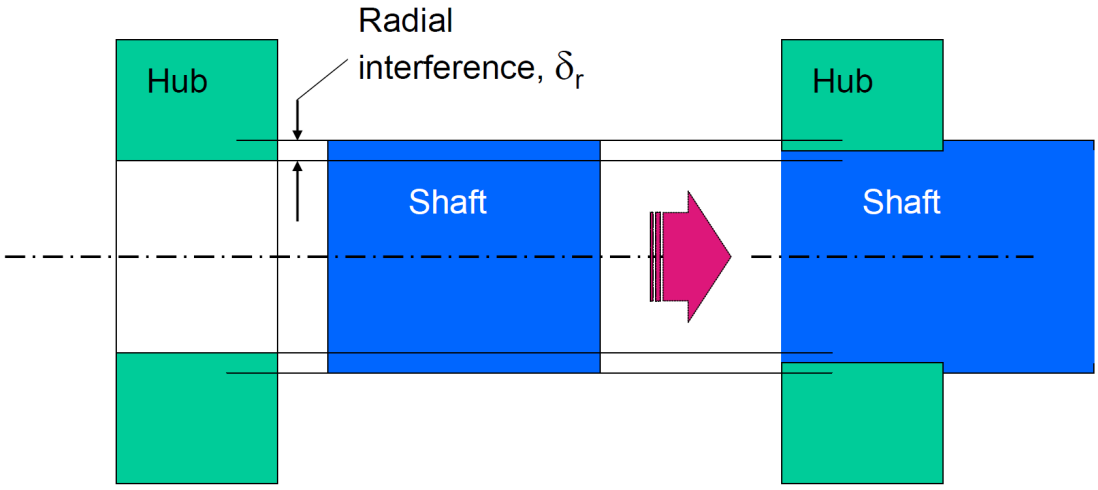

Figure 19. Principle of radial interference fit [14]

When the radial interference is known, the affecting pressure between two circular parts can be calculated. Fig. 20 presents the interference fit for two parts made of different materials. If the shaft is solid, as seen in Fig. 19, then $r_i = 0$. The following equation describe the interference pressure for two different materials [14]:

$$p_i = \frac{\delta_r}{\frac{r_f}{E_o}\left(\frac{r_o^2 + r_f^2}{r_o^2 - r_f^2} + \nu_o\right) + \frac{r_f}{E_i}\left(\frac{r_f^2 + r_i^2}{r_f^2 - r_i^2} - \nu_i\right)} \tag{5}$$

where p_i is the interference pressure, δ_r is the interference fit, r_f is the radius of interference, r_o is the outer radius, r_i is the inner radius, E_o is the elastic modulus of outer material, ν_o is Poisson's ratio of outer material, E_i is the elastic modulus of inner material and ν_i is the Poisson's ratio of inner material.

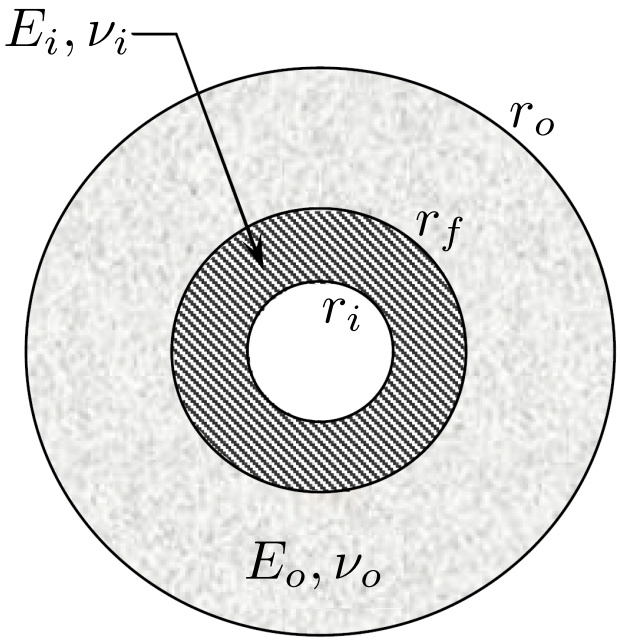

Figure 20. Interference fit with different materials [14]

The interference pressure for two part contact made of the same materials can be calculated as follows [14]:

$$p_i = \frac{E\delta_r}{r_f}\left(\frac{\left(r_o^2 - r_f^2\right)\left(r_f^2 - r_i^2\right)}{2r_f^2\left(r_o^2 - r_i^2\right)}\right) \tag{6}$$

where p_i is the interference pressure, E is the elastic modulus, δ_r is the interference fit, r_f is the radius of interference, r_o is the outer radius and r_i is the inner radius.

2.5.2 Stresses in interference fit

An interference fitted sleeve can be either a thin-walled sleeve or a thick-walled sleeve. The equations for different stress components are dependent on the relative wall thickness of the sleeve, therefore, classification is compulsory. Equations which determine if the sleeve is either thin or thick-walled are as follows [13]:

$$\frac{d_i}{t_h} > 40 \tag{7}$$

$$\frac{d_i}{t_h} \leq 40 \tag{8}$$

where d_i is the inner diameter of a sleeve and t_h is the wall thickness.

Eq. 7 describes the definition of a thin-walled sleeve and Eq. 8 describes the definition of a thick-walled sleeve. The radial and tangential stresses for a thin-walled sleeve can be calculated as follows [15]:

$$\sigma_r = -p_i \tag{9}$$

$$\sigma_t = \frac{p_i r_f}{t_h} \tag{10}$$

where σ_r is the radial stress, p_i is the interference pressure, σ_t is the tangential stress, r_f is the radius of interference and t_h is wall thickness.

With thin-walled sleeve interference, the radial stress is equivalent to the interference pressure according to Eq. 9. The tangential stress, also knows as circumferential stress or hoop stress, can be calculated using Eq. 10. Respectively, the radial and tangential stresses for thick-walled sleeve can be calculated as follows [14]:

$$\sigma_r(r_{ref}) = \frac{r_i^2 p_i - r_o^2 p_o - (p_i - p_o)\,\dfrac{r_i^2 r_o^2}{r_{ref}}}{r_o^2 - r_i^2} \tag{11}$$

$$\sigma_t(r_{ref}) = \frac{r_i^2 p_i - r_o^2 p_o + (p_i - p_o)\,\dfrac{r_i^2 r_o^2}{r_{ref}}}{r_o^2 - r_i^2} \tag{12}$$

where σ_r is the radial stress, r_i is the inner radius, p_i is the pressure in inner radius, r_o is the outer radius, p_o is the pressure in outer radius and r_{ref} is the radius used to calculate radial or tangential stress.

With thick-walled sleeve interference, the radial stress for an arbitrary radius can be calculated using Eq. 11. Respectively, the tangential stress for an arbitrary radius can

be calculated using Eq. 12. Fig. 21 describes the impact of inner and outer pressures and different stress components.

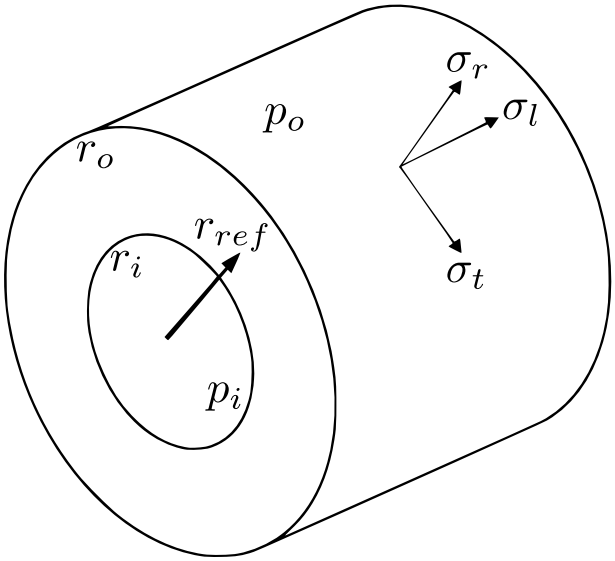

Figure 21. Stress components in interference fit [14]

In the case of $p_o = 0$ with thick-walled sleeve interference, the radial and tangential stresses can be calculated as follows [14]:

$$\sigma_r(r_{ref}) = \frac{r_i^2 p_i}{r_o^2 - r_i^2}\left(1 - \frac{r_o^2}{r_{ref}^2}\right) \tag{13}$$

$$\sigma_t(r_{ref}) = \frac{r_i^2 p_i}{r_o^2 - r_i^2}\left(1 + \frac{r_o^2}{r_{ref}^2}\right) \tag{14}$$

where σ_r is the radial stress, r_i is the inner radius, p_i is the pressure in inner radius, r_o is the outer radius and r_{ref} is the radius used to calculate radial or tangential stress [14].

2.5.3 Stresses of rotating disk

There are multiple references in literature for analytical equations of stresses formed for a circularly symmetrical rotating disk. The following equations are for radial and tangential stress [16]:

$$\sigma_r(r_{ref}) = \frac{1}{8}\rho\omega^2 (\nu + 3) \left(r_i^2 + r_o^2 - \frac{r_i^2 r_o^2}{r_{ref}^2} - r_{ref}^2 \right) \tag{15}$$

$$\sigma_t(r_{ref}) = \frac{1}{8}\rho\omega^2 \left((\nu + 3) \left(r_i^2 + r_o^2 \right) + (\nu + 3) \frac{r_i^2 r_o^2}{r_{ref}^2} - (1 + 3\nu) r_{ref}^2 \right) \tag{16}$$

where σ_r is the radial stress, ρ is the material density, ω is the angular velocity, ν is the Poisson's ratio, r_i is the inner radius, r_o is the outer radius, r_{ref} is the radius used to calculate radial or tangential stress and σ_t is the tangential stress. Fig. 22 illustrates a small disk element under centrifugal force.

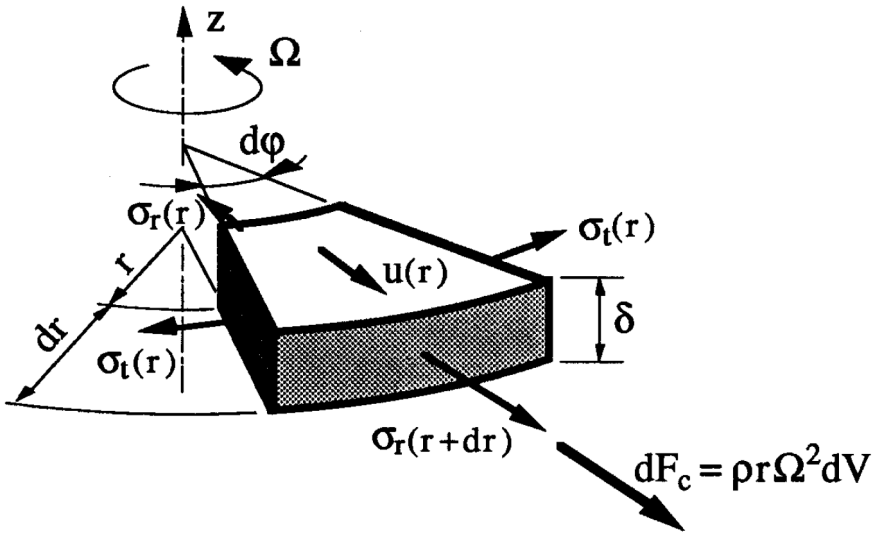

Figure 22. Small disk element under centrifugal force [16]

Fig. 23 and Fig. 24 illustrate the stress distributions of a hollow and a solid disk. Maximum stresses in the solid disk affect the center of the disk. Respectively, in the case of a hollow disk, the maximum radial stress approximately affect in the middle of

the disk and the maximum tangential stress on the inner surface of the disk.

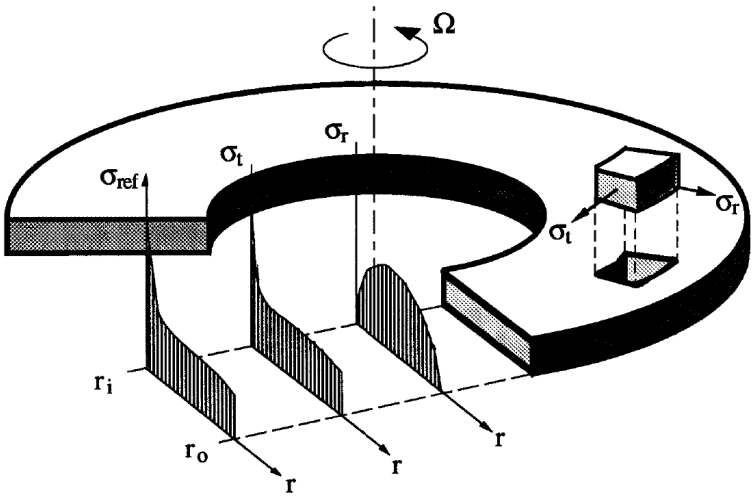

Figure 23. Stress distributions of hollow disk [16]

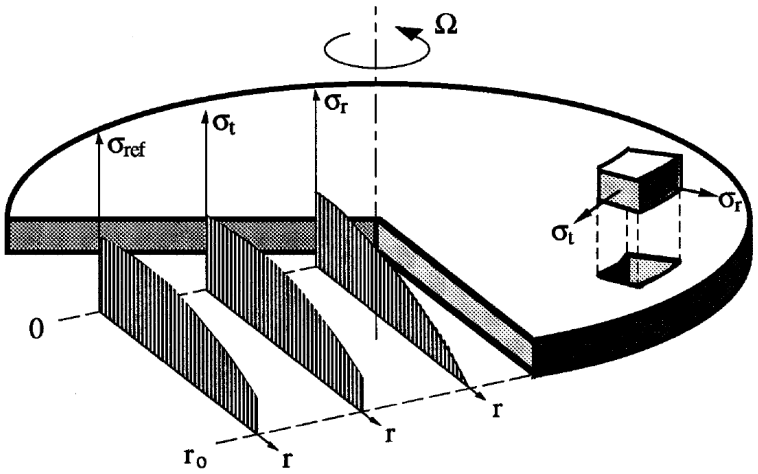

Figure 24. Stress distributions of solid disk [16]

2.5.4 Equations for thread components

I the test rig rotor, an axial AMB disk is connected to the rotor using threads, and radial AMB lamination sleeves are also secured with spinner nuts. Therefore, the following equations are introduced in order to make an accurate finite element model of the rotor.

The frictionless axial force produced by thread geometry can be calculated as follows [17]:

$$F_a = \frac{T_t}{\mu_{th} d_m} \tag{17}$$

where F_a is the axial force or tension force of the fastening component, T_t is the tightening torque, μ_{th} is the friction coefficient of thread, with steel to steel contact $\mu_{th} = 0.2$, and d_m is the major diameter of the thread [17]. Due to the axial force of the thread connection, torque that is trying to loosen the contact can be calculated as follows [18]:

$$T_{ls} = \frac{F_a p}{2\pi} \tag{18}$$

where T_{ls} is the loosening torque, F_a is the axial force and p is the thread pitch. Frictional force that keep thread contact fastened can be calculated as follows [18]:

$$T_\mu = F_a \left(\frac{\mu_{th} d_p}{2 \cos\left(\frac{\alpha}{2}\right)} + \frac{\mu_a d_{avg}}{2} \right) \tag{19}$$

where T_μ is the friction torque, F_a is the axial force, μ_{th} is the friction coefficient of thread, d_p is the pitch diameter, α is the flank angle, μ_a is the friction coefficient in the axial direction between the nut base and the friction surface and d_{avg} is the average diameter of nut base and friction surface; this dimension is not standardized if the fastening component is custom made, for example a thread sleeve in axial disk. The thread connection will not loosen if $T_{ls} < T_\mu$ [18]. Fig. 25 shows main dimension used in Eq. 17–19.

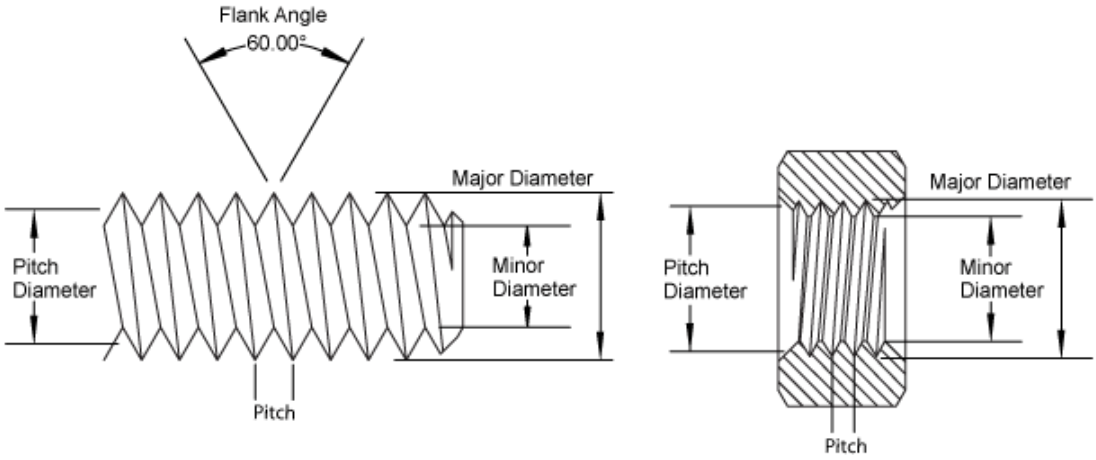

Figure 25. Main dimensions of ISO metric screw thread [19]

By taking into account surface friction forces, the total axial force can be expressed as follows [20]:

$$F_a = \frac{T_t}{0.16p + 0.582\mu_{th}d_p + \mu_a r_{avg}} \tag{20}$$

where F_a is the axial force, T_t is the tightening torque, p is the thread pitch, μ_{th} is the friction coefficient of thread, d_p is the pitch diameter, μ_a is the friction coefficient in the axial direction between the nut base and the friction surface and r_{avg} is the average radius of the nut base and the friction surface. The accuracy of Eq. 20 is dependent on the used friction coefficients which can be hard to determine accurately.

2.6 Rotordynamics

Rotordynamics studies the dynamics of rotating machinery. Special features in rotordynamics compared to structural vibration analysis are gyroscopic moments, cross-coupled forces, and the possibility of whirling instability. According to Chen and Gunter [21] the main objectives of designing and analysing rotor structure using rotordynamics are:

- predicting critical speeds when due to unbalance rotor vibration is at maximum,
- determining design modifications in order to change critical speeds. If it is

necessary to change the operational speed of a machine, design modifications may be required to change the critical speeds,

- calculating balancing masses and locations according to the measured vibration data. This way, the amplitude of synchronous vibration can be reduced,
- predicting the amplitudes of synchronous vibration caused by rotor unbalance. This is very difficult to perform accurately because the amplitude of whirling depends on the distribution of imbalance along the rotor and the rotor-bearing system damping,
- predicting the threshold speeds and vibration frequencies for dynamic instability. This objective is also difficult to accomplish because a number of the destabilizing forces are still not understood well enough to make an accurate mathematical model. However, the instability caused by journal bearings, called oil whip, can be predicted quite accurately.
- determining design modifications in order to suppress dynamic instabilities. Computer simulations can predict the relative stabilizing effect of various hardware modifications; this can be done even if the models for destabilizing force are only approximations.
- providing the accurate physical models used in the identification, model based control design and validation of control design simulations. Typically, the models used in the control design and identification include only one to three first rotor bending modes.

According to Kärkkäinen [9] a generalized matrix form of the equation of motion for rotor-bearing system using beam elements can be presented as follows :

$$\boldsymbol{M}\ddot{\boldsymbol{q}} + (\boldsymbol{C} + \Omega\boldsymbol{G})\,\dot{\boldsymbol{q}} + \left(\boldsymbol{K} + \frac{1}{2}\dot{\Omega}\boldsymbol{G}\right)\boldsymbol{q} = \Omega^2\boldsymbol{Q}_1 + \dot{\Omega}\boldsymbol{Q}_2 + \boldsymbol{F} \tag{21}$$

where $\boldsymbol{M}$ is the mass matrix, $\boldsymbol{q}$ is the vector of nodal coordinates, $\boldsymbol{C}$ is the damping matrix, Ω is the rotational speed, $\boldsymbol{G}$ is the gyroscopic matrix, $\boldsymbol{K}$ is the stiffness matrix and $\boldsymbol{F}$ is the vector of externally applied forces. The unbalance force vector of the rotor related to constant rotational speed of the rotor $\boldsymbol{Q}_1$ and the unbalance force vector of the rotor related to acceleration of the rotor $\boldsymbol{Q}_2$ are described as follows [9]:

$$\boldsymbol{Q}_1 = \begin{bmatrix} \boldsymbol{q}_1^c & \boldsymbol{q}_2^c & \cdots & \boldsymbol{q}_n^c \end{bmatrix}^{\mathrm{T}} \tag{22}$$

$$\boldsymbol{Q}_2 = \begin{bmatrix} \boldsymbol{q}_1^{nc} & \boldsymbol{q}_2^{nc} & \cdots & \boldsymbol{q}_n^{nc} \end{bmatrix}^{\mathrm{T}} \tag{23}$$

where $\boldsymbol{Q}_1$ is the unbalance force vector of the rotor related to constant rotational speed of the rotor, $\boldsymbol{Q}_2$ is the unbalance force vector of the rotor related to constant rotational speed of the rotor and n is the number of nodes. The unbalance vectors $\boldsymbol{q}_i^c$ and $\boldsymbol{q}_i^{nc}$ of the node i at the time t can be defined as follows [9]:

$$\boldsymbol{q}_i^c = \begin{bmatrix} m_{ub} e_{ub} \cos(\Omega t + \alpha) \\ m_{ub} e_{ub} \sin(\Omega t + \alpha) \\ 0 \\ 0 \end{bmatrix} \tag{24}$$

$$\boldsymbol{q}_i^{nc} = \begin{bmatrix} m_{ub} e_{ub} \sin(\Omega t + \alpha) \\ -m_{ub} e_{ub} \cos(\Omega t + \alpha) \\ 0 \\ 0 \end{bmatrix} \tag{25}$$

where $\boldsymbol{q}_i^c$ is the unbalance vector related to constant speed, m_{ub} the mass of the unbalance, e_{ub} is the eccentricity of the unbalance, t is time, α is the phase angle of the unbalance and $\boldsymbol{q}_i^{nc}$ is the unbalance vector related to acceleration. Fig. 26 presents the unbalance forces of the decelerating rotor at node *i* ($\dot{\Omega} < 0$) [9].

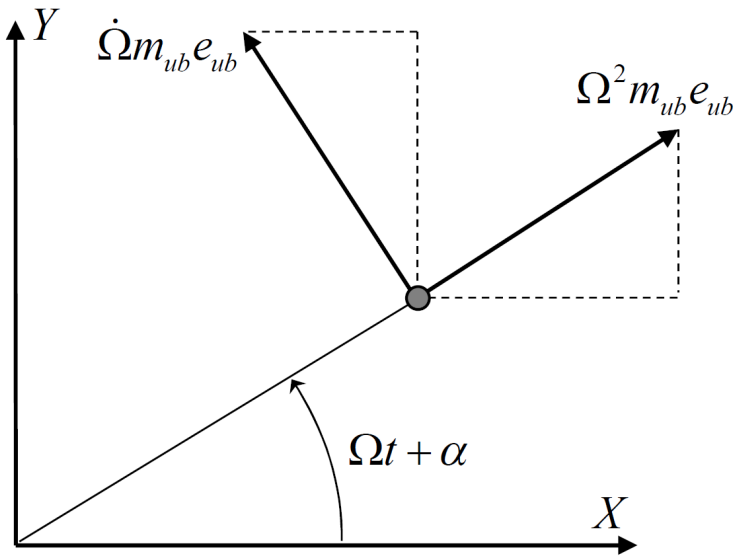

Figure 26. Unbalance forces of deceleration rotor at node *i* [9]

If the rotational speed is constant, Eq. 21 can be simplified as follows [9]:

$$\boldsymbol{M}\ddot{\boldsymbol{q}} + (\boldsymbol{C} + \Omega\boldsymbol{G})\,\dot{\boldsymbol{q}} + \boldsymbol{K}\boldsymbol{q} = \Omega^2\boldsymbol{Q}_1 + \boldsymbol{F} \tag{26}$$

where $\boldsymbol{M}$ is the mass matrix, $\boldsymbol{q}$ is the vector of nodal coordinates, $\boldsymbol{C}$ is the damping matrix, Ω is rotational speed, $\boldsymbol{G}$ is the gyroscopic matrix, $\boldsymbol{K}$ is the stiffness matrix, $\boldsymbol{Q}_1$ is the unbalance force vector of the rotor related to constant rotational speed of the rotor and $\boldsymbol{F}$ is the vector of externally applied forces.

3 DESIGN OF RECONFIGURABLE TEST RIG

The design iteration process of the reconfigurable test rig is presented in this section. Rotor design consist of general dimensioning, material selections, interference calculations and FEA verifications. The concept design of modules includes material selections in order to ensure suitable flux insulations for magnetic components. Reconfigurability enables the possibility to use the same or new modules in different configurations later on.

3.1 Overview of reconfigurable test rig

Test rig design consists of an induction machine, two sets of radial AMB modules and one axial AMB module as seen in Fig. 27. Safety bearings are attached along the AMB modules. The concept design process started by designing electrical components and taking into account space and magnetic insulation requirements. When all the needed dimension for the electrical components were defined, the mechanical design was performed for the shaft and module frames.

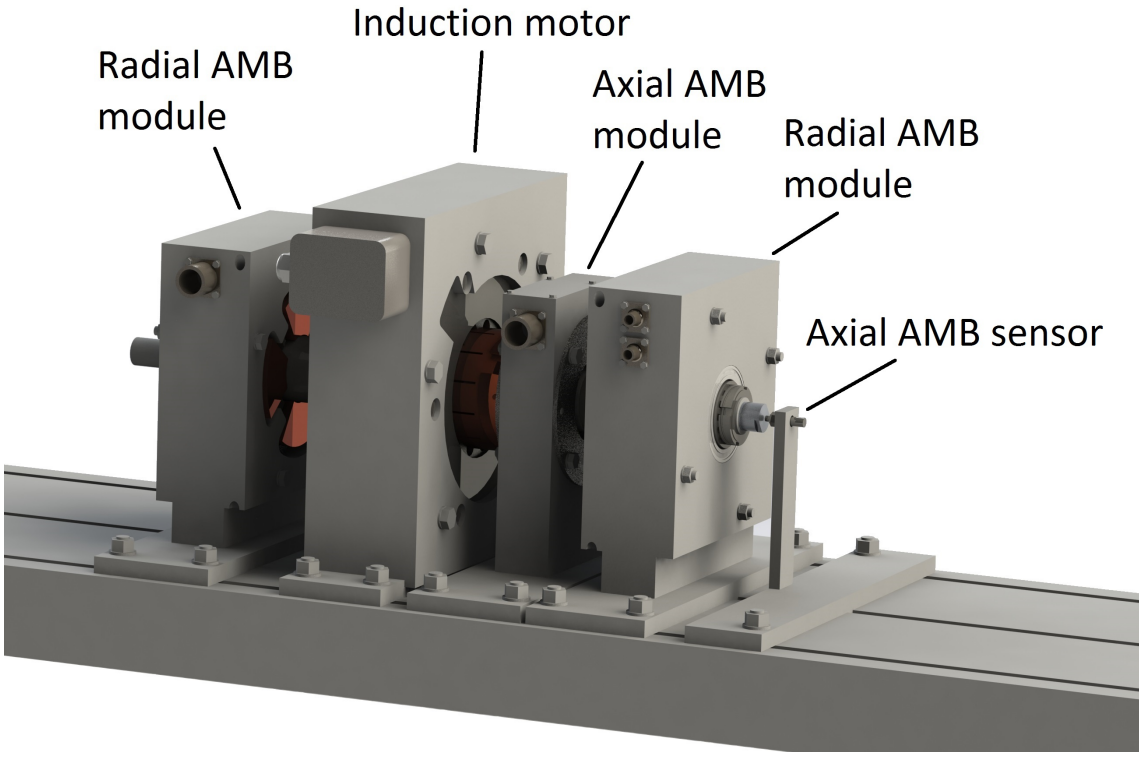

Figure 27. Initial concept design of reconfigurable test rig

3.2 Design specifications

The design studied in this thesis is the first configuration of a reconfigurable test rig project, which consists of three different types of AMB designs. The design process of the test rig was initiated by defining the design specifications. A major part of specifications presented in Table 1 are related to electrical parts, their dimensions and required air gaps. Due to new ideas during the design process, some specifications needed to be redefined. The process of selecting the proper radial safety bearings defined the finalized radial lamination dimensions. In addition, the axial AMB disk OD was changed in order to reduce high centrifugal stresses. The fulfilled specifications after preliminary design are introduced in Appendix 1.

Table 1. Test rig design specifications

Rotor	
Operational speed	30 000 rpm
Shaft length	800 mm
Mass	20 kg
Balancing grade	G2.5
Rotor type	Slitted rotor
Rotor OD	68 mm
Rotor length	80 mm
Radial AMB rotor lamination OD	55 mm
Axial AMB disk	Solid magnetic steel disk
Axial AMB disk OD	120 mm
Induction motor	
IM power	10 kW
Stator inner diameter	70 mm
IM stator air gap	1.0 mm
Bearings	
Radial AMB stator	E-core lamination
Radial stator inner diameter	56 mm
Radial AMB air gap	500 µm
Radial SB air gap	250 µm
Radial SBs	Suitable deep groove ball bearings
Axial AMB stator	Solid magnetic steel stators
Axial AMB air gap	1.0 mm
Axial SB air gap	500 µm
Axial SBs	Brass retainer rings
Base plate and frame structure	
Base plate length	2 000 mm

3.3 Rotor

The test rig rotor consists of a slitted IM rotor, multiple shoulders for radial and axial AMBs and also a support for mechanical safety bearings, sensor surfaces and a shoulder

for possible high speed coupling for the impeller. Fig. 28 presents the initial concept design of the rotor assembly.

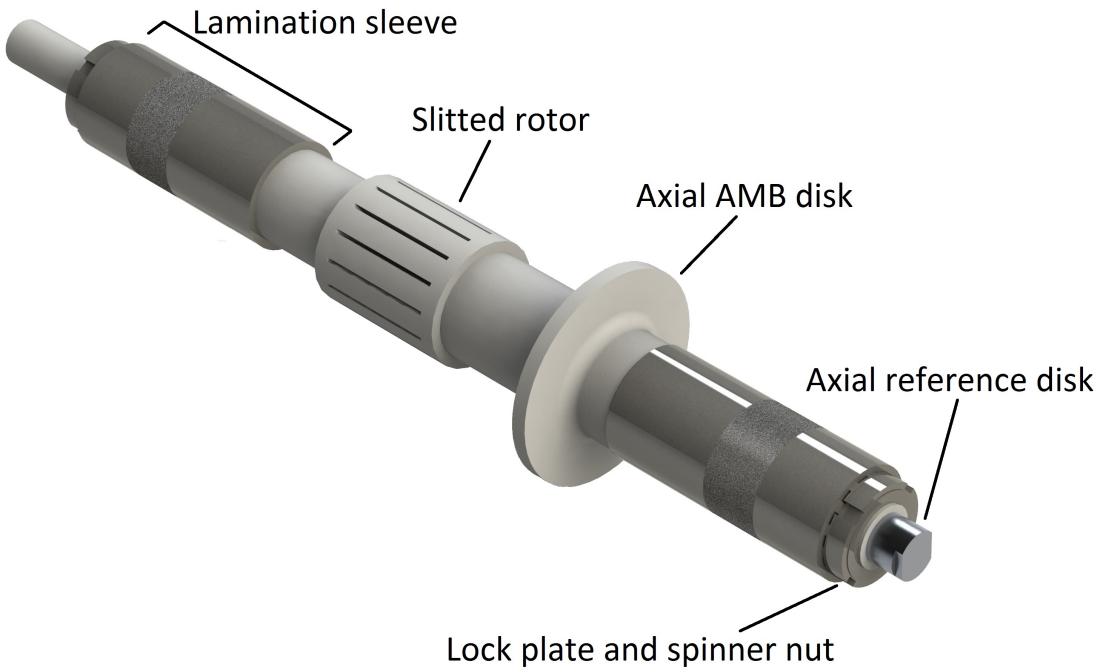

Figure 28. Test rig rotor with replaceable lamination sleeves

The rotor consists of three main parts; a shaft with slitted rotor of IM, an axial AMB disk and preassembled rechangeable laminations sleeves. The axial space requirement for the end windings of the radial AMB coils and IM stator required more space than originally was designed. Therefore, the rotor was lengthened by almost 30 cm from the original minimum length. In addition, replaceable safety bearing sleeves were added to design. A detailed structure of the lamination sleeve is introduced in Section 3.3.2.

3.3.1 Material selections

Almost every part related to electromagnetic performance has to be optimized according to its material properties. For an rotor of IM, the optimum material is magnetic steel, in this case typical structural steel S355. On the other hand the optimal material for rest of the the rotor would be non-magnetic steel. This is because of optimizing AMB performance and preventing the rotor heating caused by eddy current leakage to the shaft material.

The initial design was to make a rotor part using magnetic steel and rest of the shaft using non-magnetic steel. Despite the fact that the structure would be optimal considering electromagnetic performance, making the shaft from multiple parts was not rational considering the mechanical durability. Therefore, a compromise was needed in order to ensure mechanical durability. It was decided to make the shaft one solid part using magnetic steel. Of course, this leads to a new problem of how to isolate the rotor laminations from the shaft. A lamination sleeve structure was implemented, using non-magnetic steel around the laminations except for the reference sensor surface. For particular sensor used, the surface material needs to be magnetic in order to ensure proper functionality of the sensor. This structure increases the number of parts but also enables the possibility of replaceable sleeves. Fig. 29 illustrates the slitted rotor structure. All the construction materials used in the rotor are listed in Table 2.

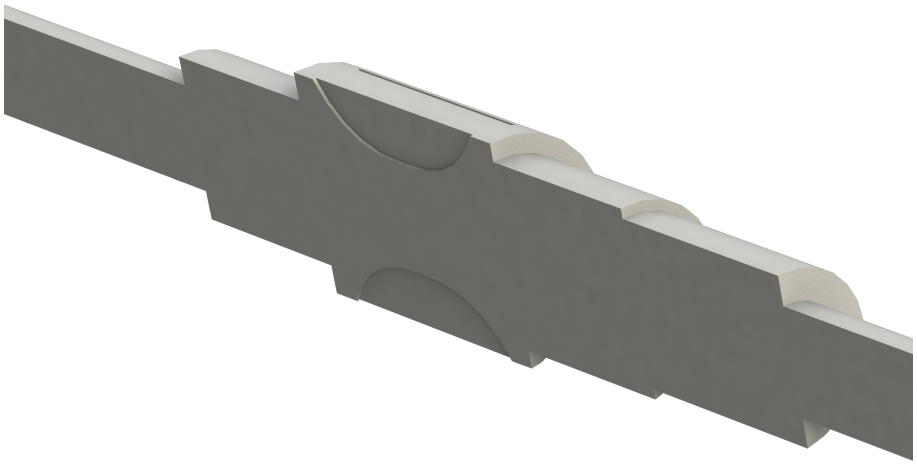

Figure 29. Section view of slitted rotor

Table 2. Rotor materials

Part	**Material**
Shaft	S355J2+N
Axial disk	S355J2+N
Lamination tubing	AISI 304
Reference sensor sleeve	42CrMo4
Laminations	M270-35A, thickness 0.35 mm
Safety bearing sleeve	S355J2+N

3.3.2 Radial AMB lamination sleeve

Due to the fact that the rotor is made of magnetic material, the radial AMB laminations require flux insulation. This is done by using the lamination tubing presented in Fig 30. Also, for reconfigurable purposes, the laminations and reference measurement surface, as well as the safety bearing contact surface, is designed to be replaceable if needed. This preassembled package is called lamination sleeve, and it can be removed as one part. The safety bearing contact surface determines the air gap to the safety bearings. It also directly affects to the design of radial AMB stator laminations.

For attaching the lamination tubing onto the rotor, a minor shrink fit is applied in addition to axial fastening using a lock plate and spinner nut. A shrink fit is needed to prevent any free radial movement of the components at high speeds. Optimum results occur when a minor negative pressure is maintained between the shaft and laminations sleeve at high speed. Respectively, this radial stress can be relatively high when the rotor is not rotating. Fig. 30 presents the design of preassembled replaceable lamination sleeve on the rotor.

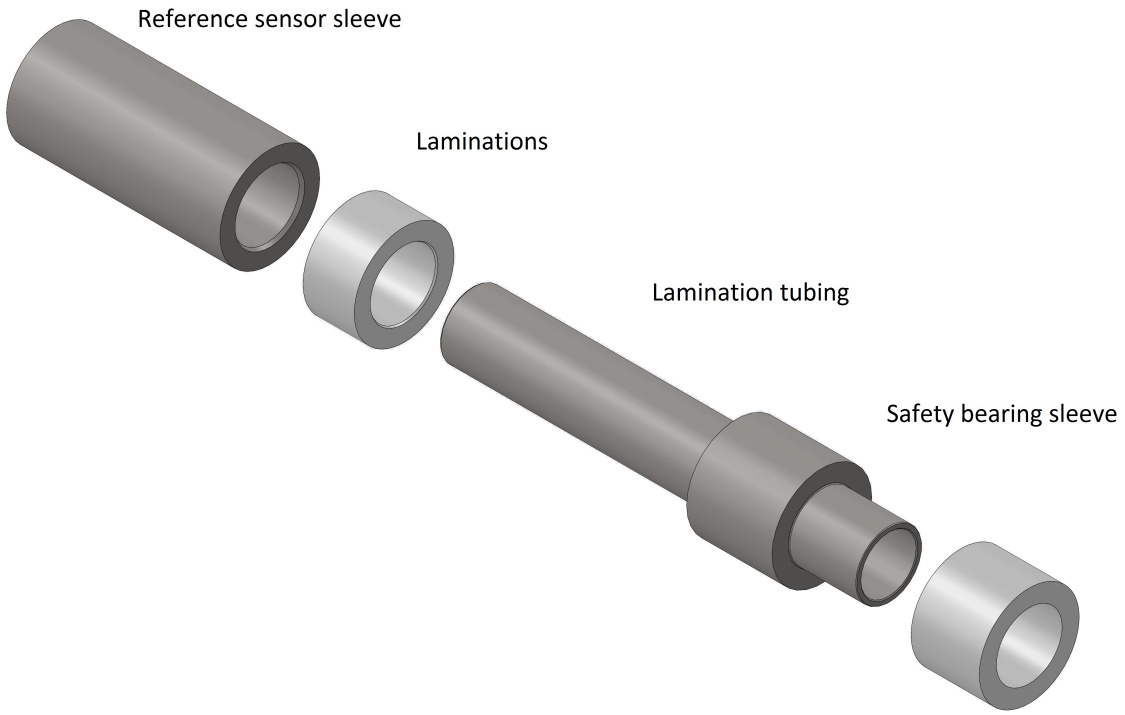

Figure 30. Updated sleeve assembly

The reference sensor surface needs to be as close as possible to the radial AMB

coils in order to minimize non-collocation, and to decrease overall footprint and size. Furthermore, the surface material can be non-magnetic but in order to ensure the best functionality of the sensor, the surface material should be magnetic steel. The original material selected was non-magnetic steel AISI 304, which was later changed to magnetic steel AISI 4140 for optimizing the signal quality of the reference sensor. The functionality of the sensor with different materials will be introduced in section 3.4.4. Detaching the lamination sleeve is possible because the outer diameter of the lamination sleeve is larger than a shoulder after the lamination sleeve. Therefore, the lamination sleeve can simply be pulled out. In addition, a groove is also added to the SB sleeve; therefore, it is also easy to replace if needed.

For reconfiguration purposes, the radial AMB laminations and the reference sensor surface are designed to be replaceable. The initial design was to use shrink fits to attach a separate lamination part to the rotor. However, this design is not practical considering the need to change the parts after. Therefore, these parts are designed to be as one pre-assembled lamination sleeve that can be fastened onto the shaft using a lock plate and spinner nut. Because of the air gap in the axial bearings, this additional movement is taken into account in the length of the rotor lamination stack and also in the safety bearings sleeve.

3.3.3 Rotor axial AMB disk

The axial disk for an axial AMB module is the most critical considering mechanical durability. As seen in Fig. 28, the largest outer diameter also causes the highest centrifugal stresses to this part. The first iteration was to relocate the disk to the other end of the rotor. Considering assembling capability, the location was not ideal. For balancing reasons, it is not practical to disassemble the disk for every new configuration. Therefore, the disk was located next to the induction motor. Now, reconfiguration of the test rig is possible without removing the axial AMB disk. To support the disk in the axial direction, a 3 mm thick sleeve is added on both sides of the disk. This construction is attached to the shaft using M42x1.5 thread. Also, by applying additional thread locking paste to the axial AMB disk threading, it can be fastened more securely.

3.3.4 Finite element analysis

Initial shrink fits are iterated using an analytical model in MATLAB. The used script by Ranft [4] is presented in Appendix 2. The principle of selecting the radial interference is to ensure negative radial pressure at the contact surfaces even at maximum operational speed. Typically, the radial pressure is multiple times higher when the rotor is not operating. Radial interference between the lamination sleeve and laminations is determined to be 15 μm, which corresponds approximately to a 65°C temperature difference using Eq. 4. The selected values for interference is higher than needed but the idea is to take possible variations in fabrication tolerances into account. In addition, no surface tolerances, surface qualities and installation tolerances have taken into account. In general, if the shrink fit is smaller, the maximum stresses are also smaller. The shrink fit contact is modelled in ANSYS using interference treatment while defining radial contacts. Shrink fit is added as an offset equal to the desired radial interference. A positive interference value indicates penetration whereas a negative value indicates an open gap. In addition, the normal stiffness factor was varied while doing sensitivity analysis for interference fit. The value of 1.0 was determined to be used for normal stiffness factor. [22]

The used materials in the finite element model and analytical model are presented in Table 3. ANSYS was used to make a full rotor assembly model. All rotor model contacts are modelled as frictional contact using a friction coefficient of 0.2. The number of elements is 389 149, the number of nodes is 773 694 and the total number of degrees of freedom (DOF) is 2 320 191. The element types used in the finite element model are SOLID187, CONTA174, TARGE170 and SURF154. A linear analysis is performed using direct solver. Due to the fact that all the used materials have the same thermal expansion properties, additional thermal effects, such as operational temperature or thermal load to the rotor, were not included in this model. Axial thermal expansion can be iterated using Eq. 4; according to the total length of the rotor, a 80°C temperature rise causes 0.86 mm lengthening. Considering the AMBs, the axial AMB disk can be used as a reference point. Therefore, maximum axial lengthening at the further radial AMB using the same temperature rise is approximately 0.41 mm.

Table 3. Material properties used in simulations [23, 24, 25, 26]

	$\rho\left[\frac{kg}{m^3}\right]$	$E\,[GPa]$	ν	$\alpha\left[\frac{1^{-6}}{K}\right]$	$R_{p0.2}\,[MPa]$	$R_m\,[MPa]$
S355J2+N	7 865	200	0.285	16.5	355	510
42CrMo4	7 865	200	0.285	16.5	550	800
AISI 304	7 865	200	0.285	16.5	215	505
M270-35A	7 600	185	0.28	16.5	450	565

The tightening of the threaded parts is modelled using axial forces. Also, the maximum possible forces are not used because circumferential forces cause additional stresses to these parts. Because of using locking paste in the case of the axial disk, the nominal axial force is iterated to be 36 kN. Using Eq. 20, the corresponding tightening torque is 406 Nm. The axial force of spinner nuts is iterated to be 18 kN, which is half of the maximum axial force of the component. According to the initial results of FEA, this value is enough. The corresponding tightening torque for spinner nuts is 132 Nm. In addition, AMB forces are added to the finite element model to maximize the stresses of the electromagnetic components. All the used loads in the finite element are presented in Table 4.

Table 4. The used loads in ANSYS rotor model

Load	**Specification**	**Finite element model**
Rotational velocity	30 000 rpm	34 000 rpm[1)]
Axial disk tightening force	406 Nm	36 000 N
Spinner nut tightening force	132 Nm	18 000 N
Lamination tubing–sleeves interference	15 µm	15 µm (44.172 MPa[2)])
Lamination tubing–lamination interference	15 µm	15 µm (41.550 MPa[2)])
Axial AMB force	127 N	191 N [3)]
Radial AMB force	282 N	423 N [3)]
[1)] with safety factor of 1.13 [2)] radial pressure at 0 rpm [3)] with safety factor of 1.5		

Detailed results of the rotor FEA using ANSYS are presented, Fig. 31 to Fig. 33 present

detailed stresses of the laminations sleeve. Fig. 34 to Fig. 36 present detailed stresses of the axial AMB disk. In addition, the stresses of the slitted rotor are presented in the same figure.

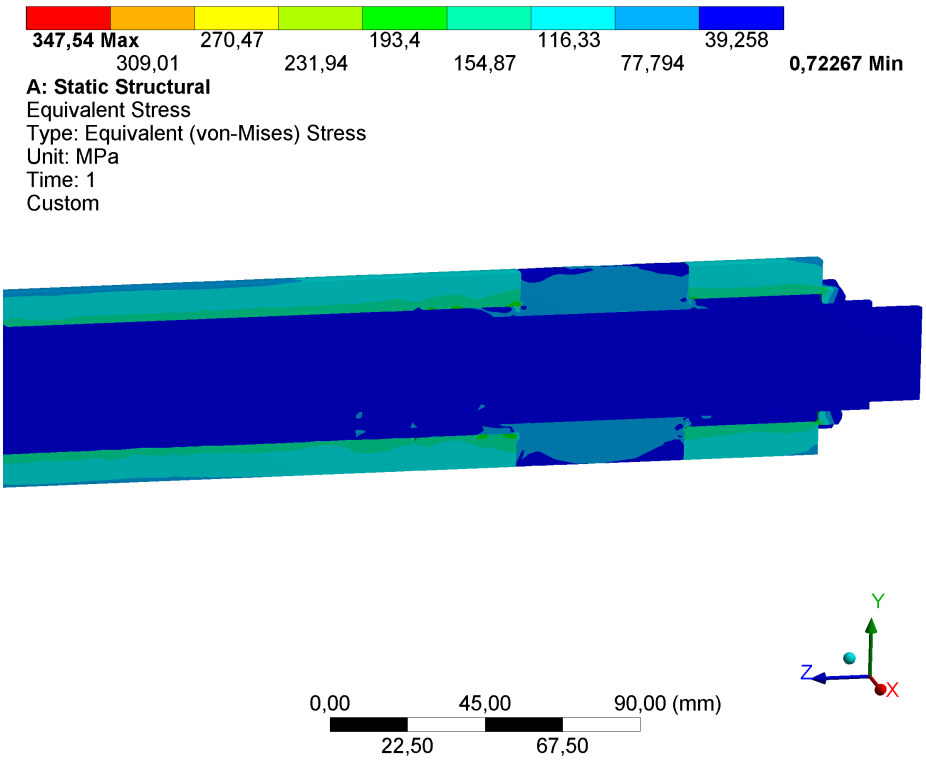

Figure 31. Sleeve equivalent stress

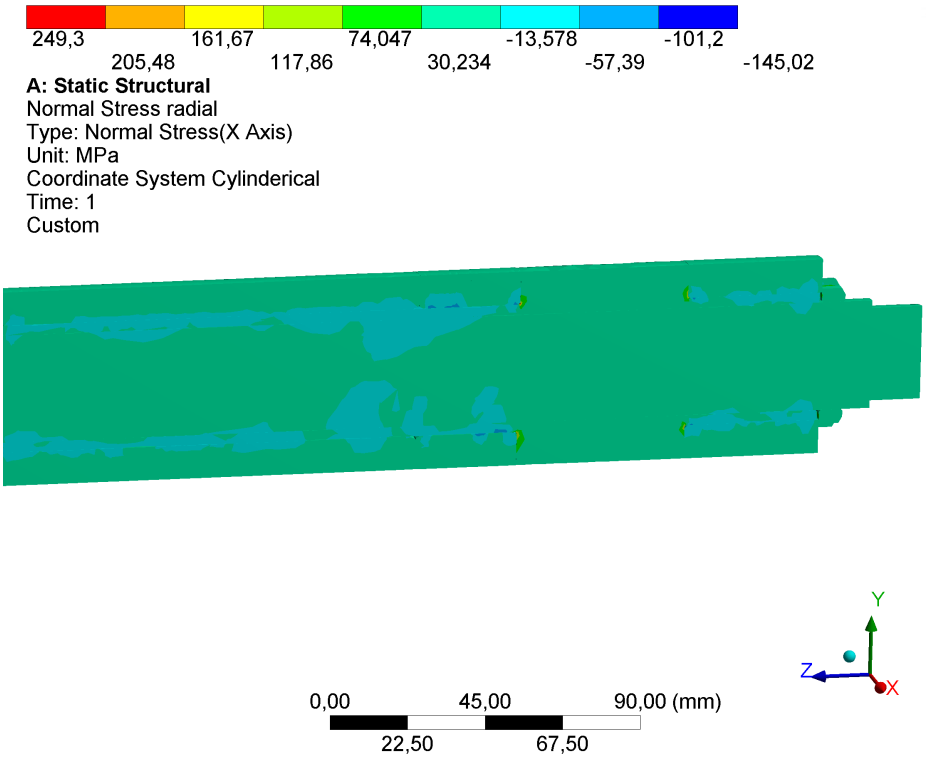

Figure 32. Sleeve radial stress

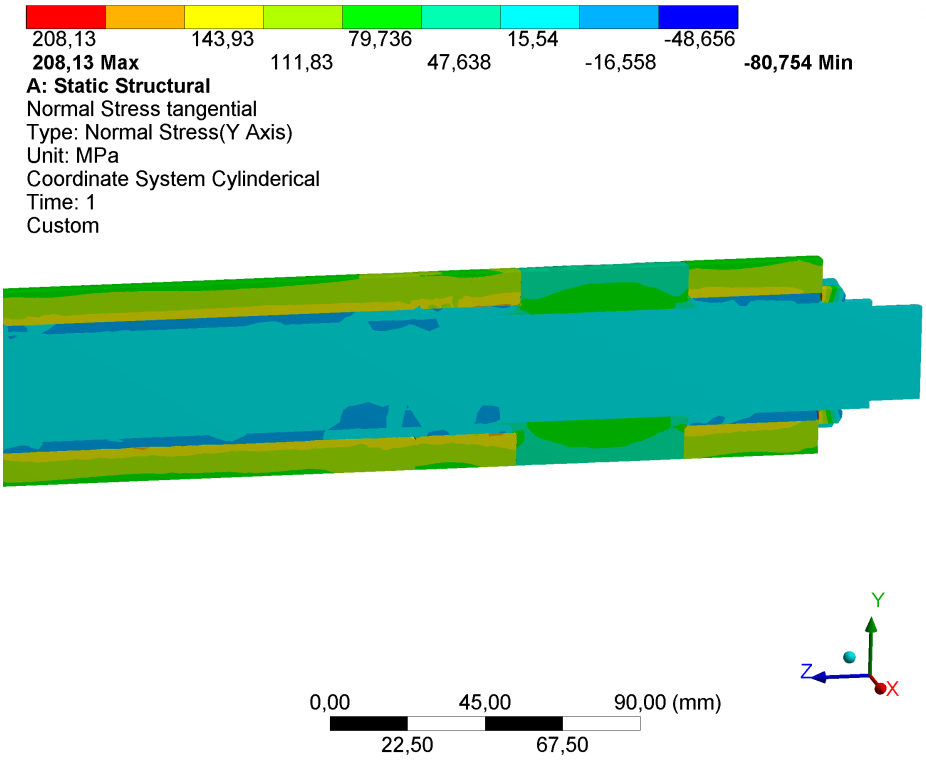

Figure 33. Sleeve tangential stress

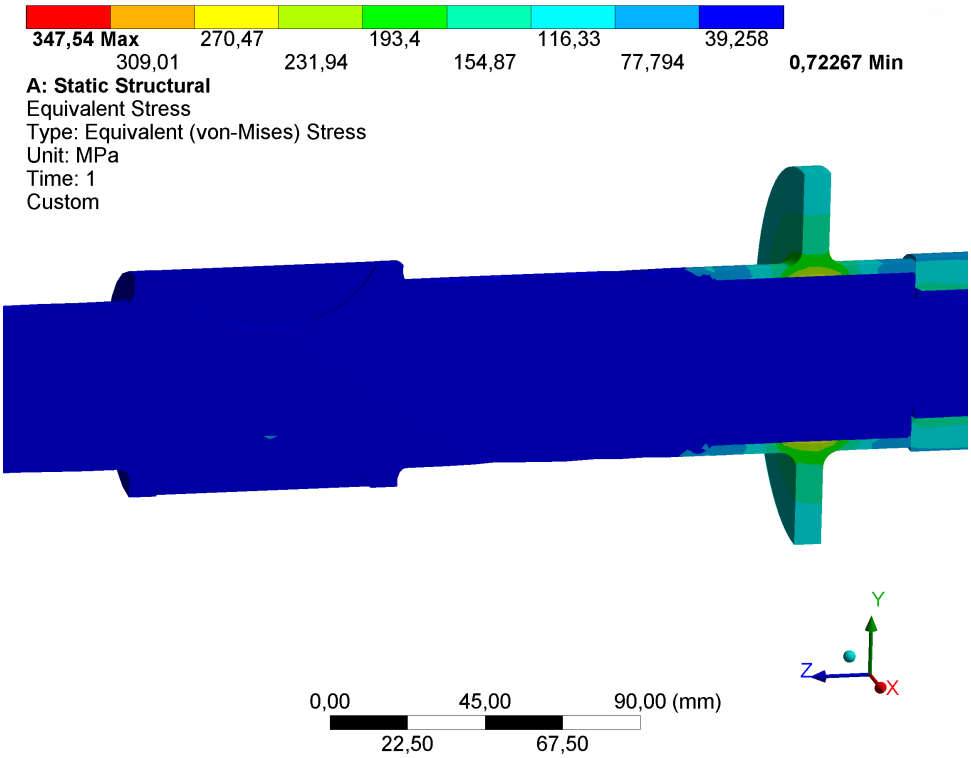

Figure 34. Axial disk equivalent stress

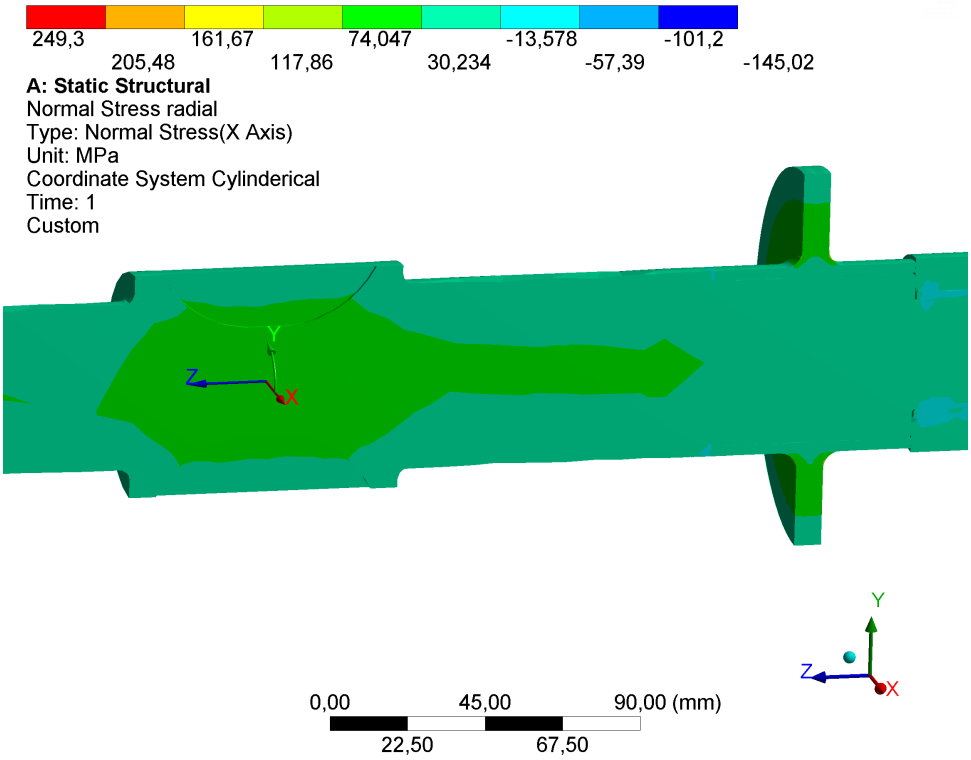

Figure 35. Axial disk radial stress

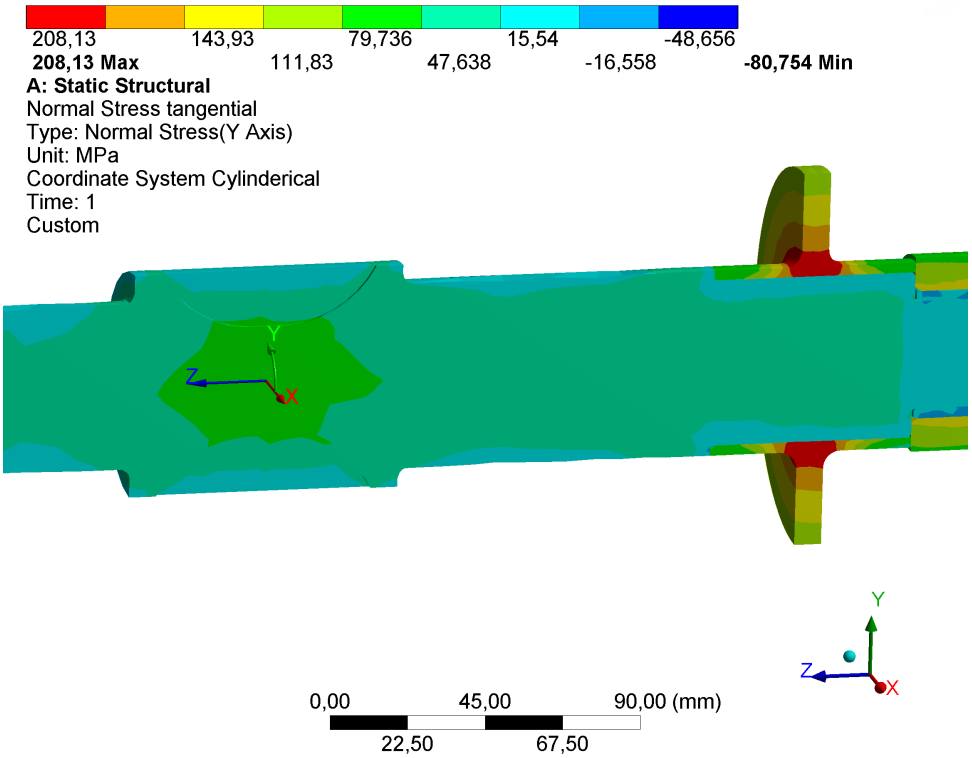

Figure 36. Axial disk tangential stress

3.3.5 Analytical results

The analytical results are generated using the MATLAB script presented in Appendix 2. The original script is modified to be suitable for simulating lamination tubing–sleeve contact. [4] Only the centrifugal load and the previously iterated shrink fit are used in this simulation. Two separate simulations were performed; Fig. 37 presents results in sleeve–sensor contact and Fig. 38 presents the results in sleeve–laminations contact.

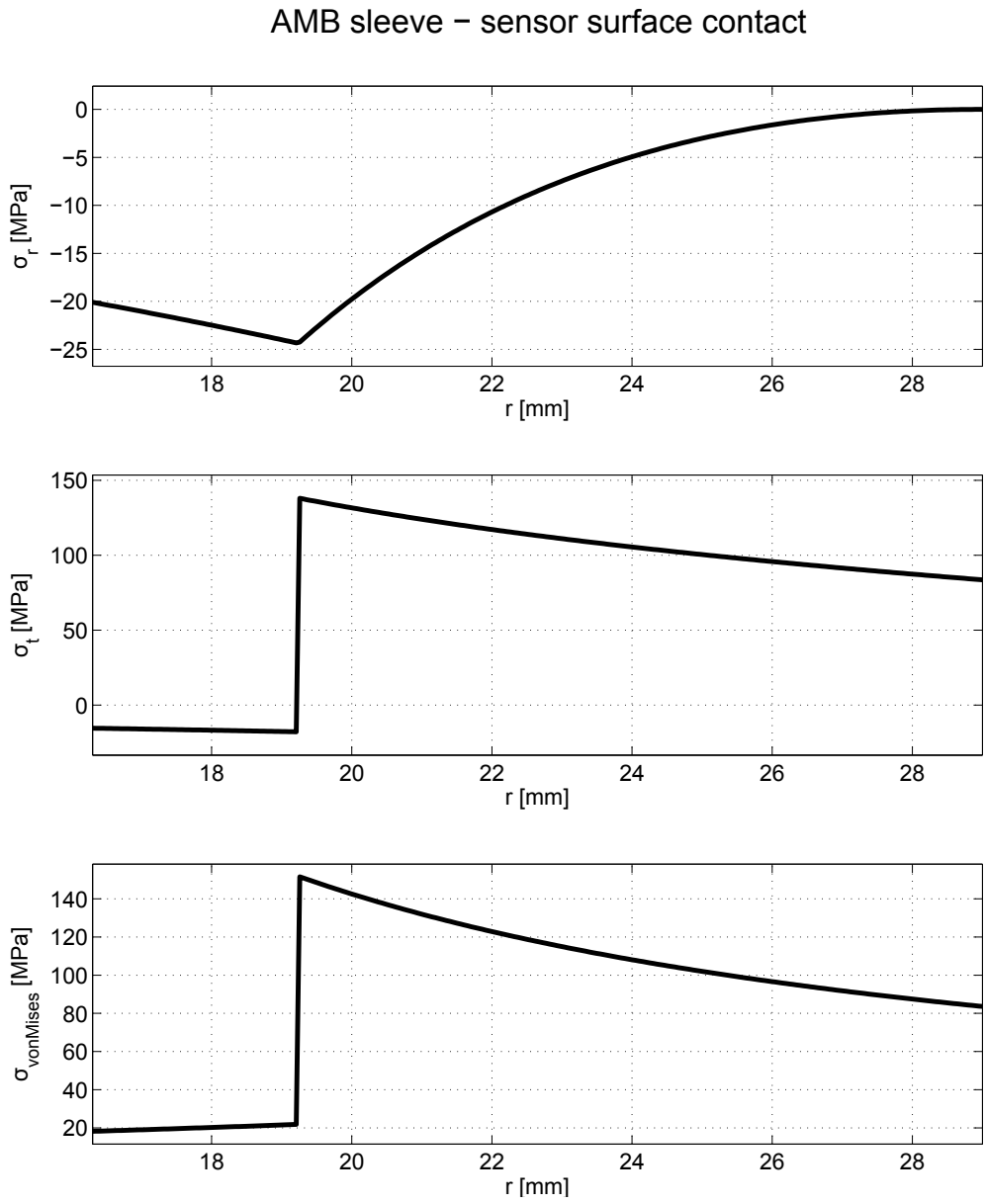

Figure 37. Analytical stresses in sleeve–sensor surface contact

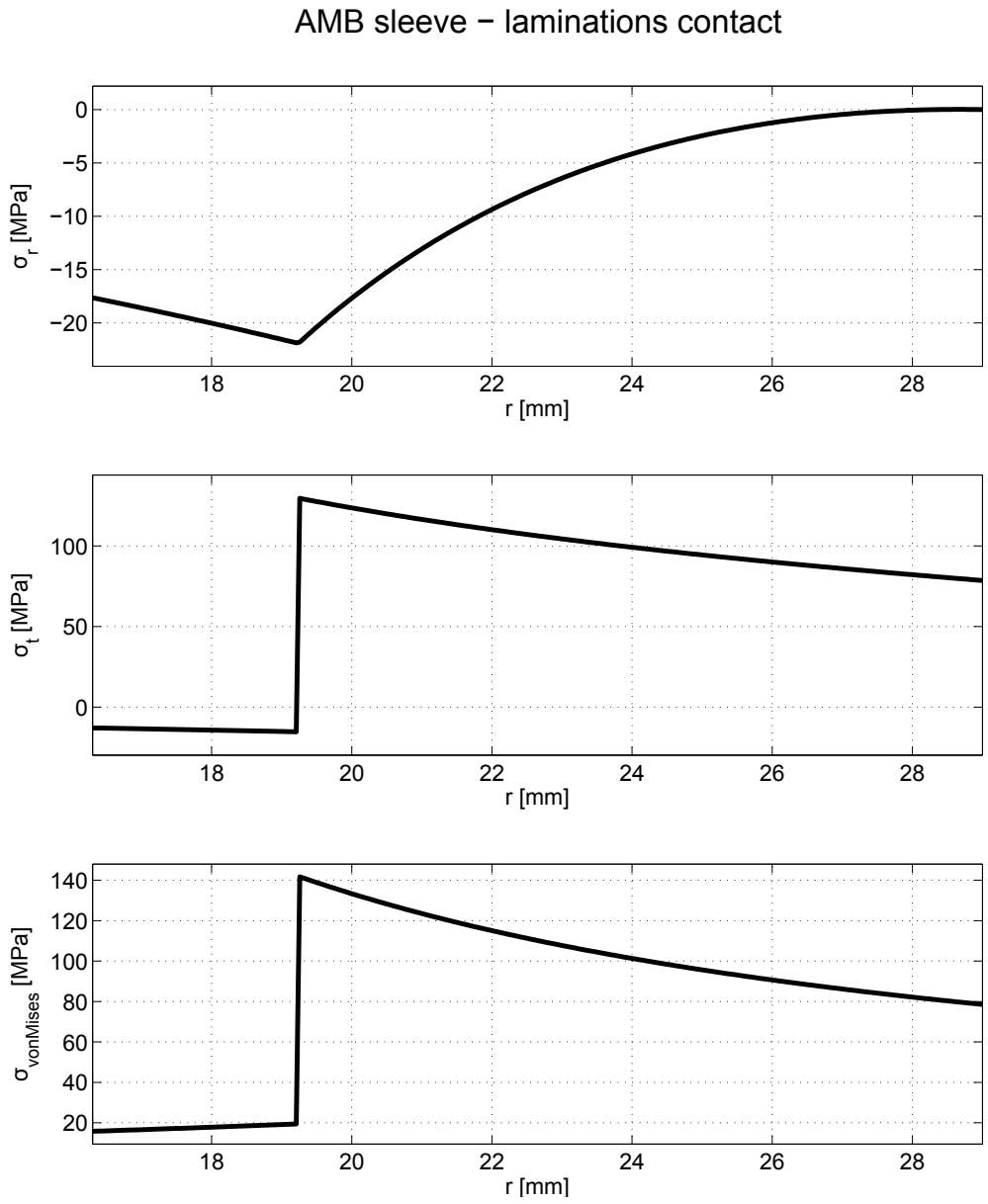

Figure 38. Analytical stresses in sleeve–laminations contact

Axial AMB disk stresses are calculated using Eqs. 11 and 12. Since the disk is connected to the rotor using threading, no contact modelling was required. The only load in the model was centrifugal force. Fig. 39 presents the radial and tangential stress of the axial disk.

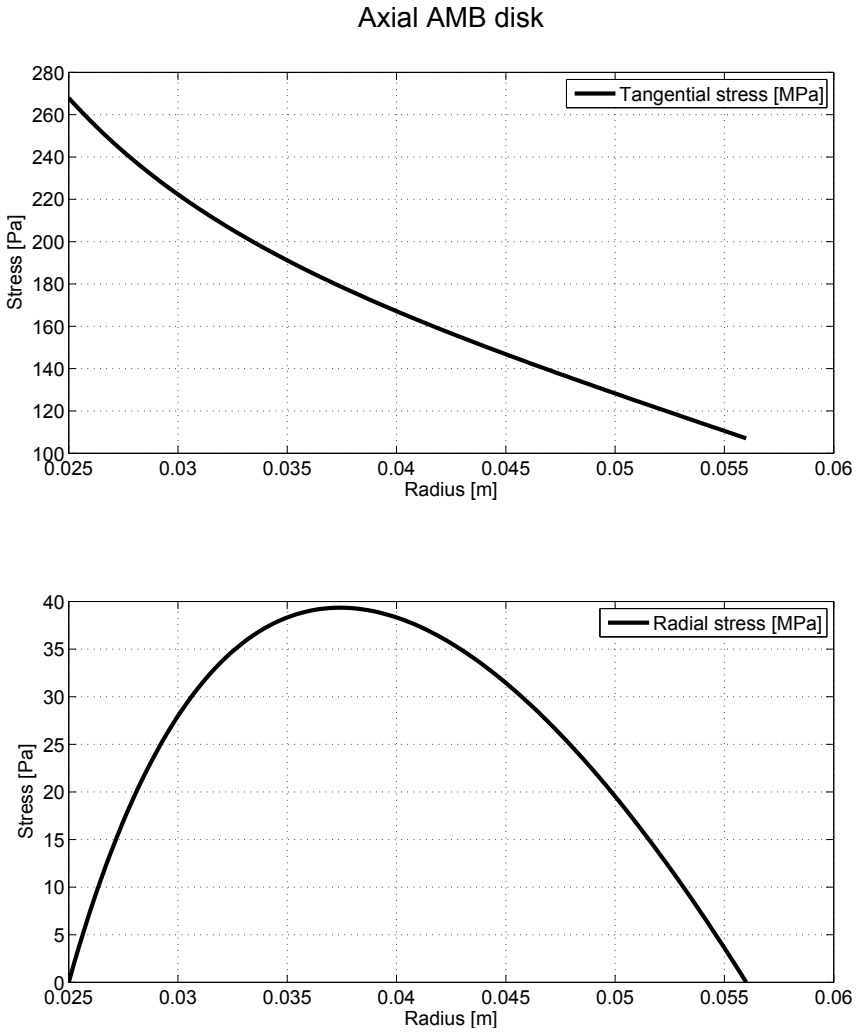

Figure 39. Analytical stresses of axial disk

3.3.6 Rotor modal analyses

The eigenmodes and -frequencies of the rotor are solved with ANSYS using solid elements and with the Rotor-Bearing Dynamics (RoBeDyn) Toolbox for MATLAB using beam elements. In addition, the fabricated rotor is also measured using automatic hammer to apply minor impulse and laser measurement equipment to detect the eigenmodes. According to a study made by Lantto [27] for validating numerical rotor model by measuring the eigenfrequencies using real rotor suggests neglecting the additional stiffness provided by laminations. In the research it was suggested modelling the laminations and impellers only as mass points and to use zero elastic modulus for these parts. According to the study the shaft–sleeve connections are not tight, especially when using different materials. The connection can get loose and then the laminations does not

contribute the rotor stiffness. [27]

An estimation is done to approximate the lamination sleeve structure behaviour. Three cases are studied: using one, twenty and fifty percent of the normal elastic modulus of the materials used in the lamination sleeve subassembly and in the axial disk while using normal density and Poisson's ratio parameters. The used material properties are introduced in section 3.3.4. A full rotor assembly model with ANSYS is done using SOLID187, CONTA174 and TARGE170 elements. The number of elements is 82 201, the number of nodes is 174 535 and the total number of DOFs is 523 404. Direct solver type and frictional contacts with a friction coefficient of 0.2 are used. Fig. 40 presents the shapes of the first two bending eigenmodes with certain deformation scale. The RoBeDyn model is generated using a 12 DOF three-dimensional beam elements and 6 DOF mass elements. Lamination sleeves are modelled as layers over the shaft. The axial AMB disk is modelled as a mass point and connected to a specific node corresponding to its position. The beam element model consists of 62 elements and total of 756 DOFs. Due to the slitted rotor design, an average diameter of 50 mm is used in modelling the slitted rotor part.

(a) First bending mode

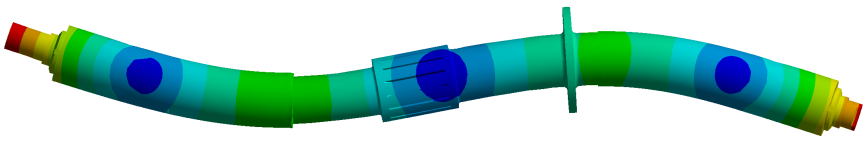

(b) Second bending mode

Figure 40. First two bending eigenmodes of the studied rotor using ANSYS

There are differences between these to presented models. First, the beam element model does not take into account the axial forces caused by the tightening torque of the spinner

nuts or the radial forces caused by the shrink fits. On the other hand, axial force modelling was tested in the solid element model but the model encountered numerical problems when using low stiffness and high load which yield high deformations in the lamination sleeve parts. Also, while using zero elastic modulus as suggested by Lantto [27] causes numerical errors in ANSYS. Therefore, the axial forces and radial shrink fit forces are not used on further studies in ANSYS in order to prove comparable results.

Secondly, the contact descriptions in the models are different. The solid element model uses frictional contacts with a friction coefficient of 0.2. In contrast, the individual parts are defined as layers with different material properties in the beam element model. Therefore, the contacts with friction between parts are not accounted for using these specific beam elements in the RoBeDyn. The measured data of the fabricated rotor is presented in Fig. 41. For comparison purposes, the measured and FEA results are compiled to Table 5.

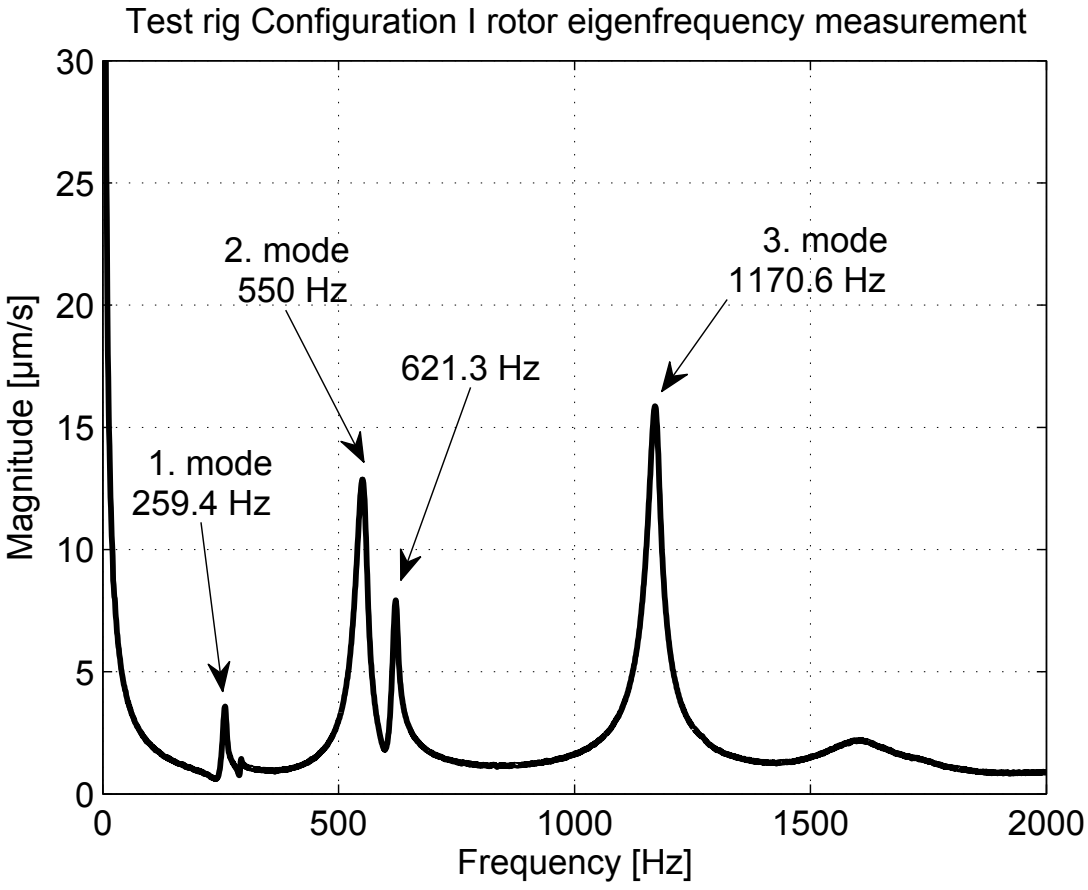

Figure 41. Measured rotor eigenfrequencies

Table 5. Results of rotor eigenfrequency studies

	1. mode		**2. mode**	
Measured	259.4 Hz		550.0 Hz	
Beam 1 % E	195.4 Hz	-24.7 %	382.9 Hz	-30.4 %
Beam 20 % E	259.0 Hz	-0.2 %	579.8 Hz	5.4 %
Beam 50 % E	303.1 Hz	16.8 %	749.2 Hz	36.2 %
Solid 1 % E	201.9 Hz	-22.2 %	380.5 Hz	-30.8 %
Solid 20 % E	268.4 Hz	3.5 %	576.3 Hz	4.8 %
Solid 50 % E	307.9 Hz	18.7 %	743.9 Hz	35.3 %

3.4 Modular actuator designs

The iteration process and concept design of stator components and modules that enables an AMB supported system are reviewed in this section. AMB stators are mounted to modules, which enables quick changes to AMB configuration. In general, a modular structure is required in order to fulfill the requirement for reconfigurability. Due to the modular construction of this test rig, some unexpected alignment issues may occur. Therefore, air gaps are selected to be larger than the optimal values. Larger air gaps also affect the windings and electromagnetic components need to be bigger in order to generate same force but from greater distance. Fig. 42 illustrates the initial concept design of the test rig layout where minor spaces between modules can be seen. These spaces were increased in the updated design in order to make space for the coil end windings.

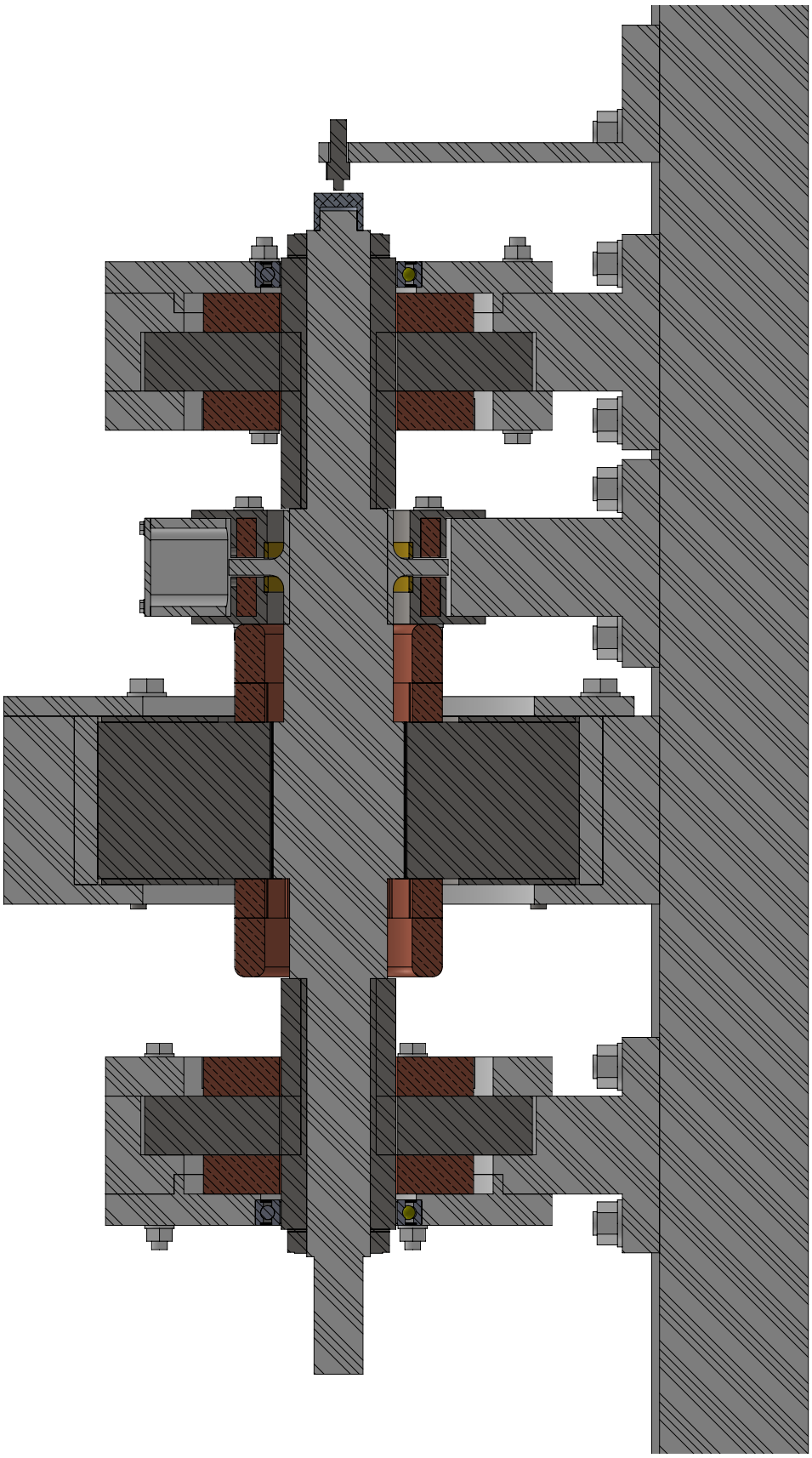

Figure 42. Cross section of concept design of the test rig

3.4.1 IM module

The test rig design iteration process started by designing the IM stator. The stator consists of 0.27 mm thick Sura NO27 electric steel lamination sheets. On both ends of the lamination stack non-magnetic end plates called finger plates are placed. These plates increase the mechanical durability by preventing bending the of the lamination sheets. Fig. 43 presents an early design of the stator with finger plates using bolt connections.

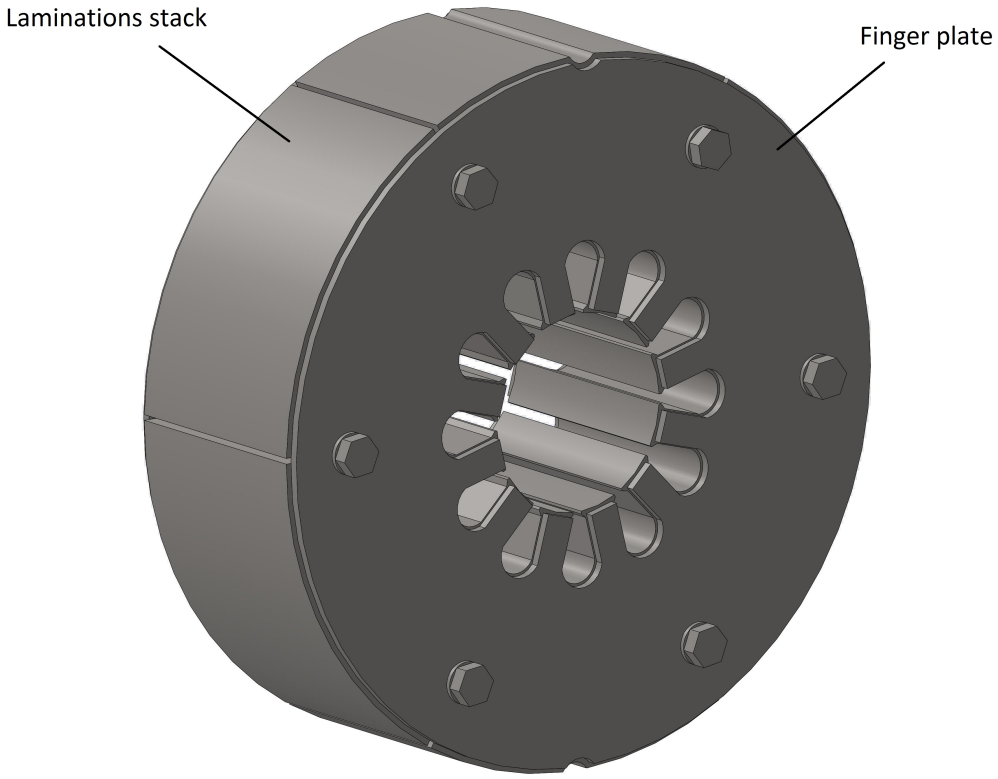

Figure 43. IM stator with finger plates

Further along, the bolt connection was replaced. By welding the stack and finger plates into one piece was a more practical solution. Also, using bolts there would have to be air gap all the way to the end of the back iron. This would cause eddy current losses in the stack. Finger plates also cause some additional eddy current losses, but for mechanical durability reasons these plates were added to the stator stack. The industrial fabricating method of lamination sheets enables better conducting properties in the rolling direction. For optimizing the electrical performance, the orientation of the lamination sheets in the stack is mixed, if possible.

3.4.2 Radial AMB module

For practical reasons, the safety bearings are located in the same module as the AMBs. To generate maximum accuracy in the controlling system, flux sensors, which work as reference sensors are located right next to the radial AMB coil windings. Radial AMB stator is in the middle of Fig. 44, on the left, a safety bearing and on the right, the reference sensors.

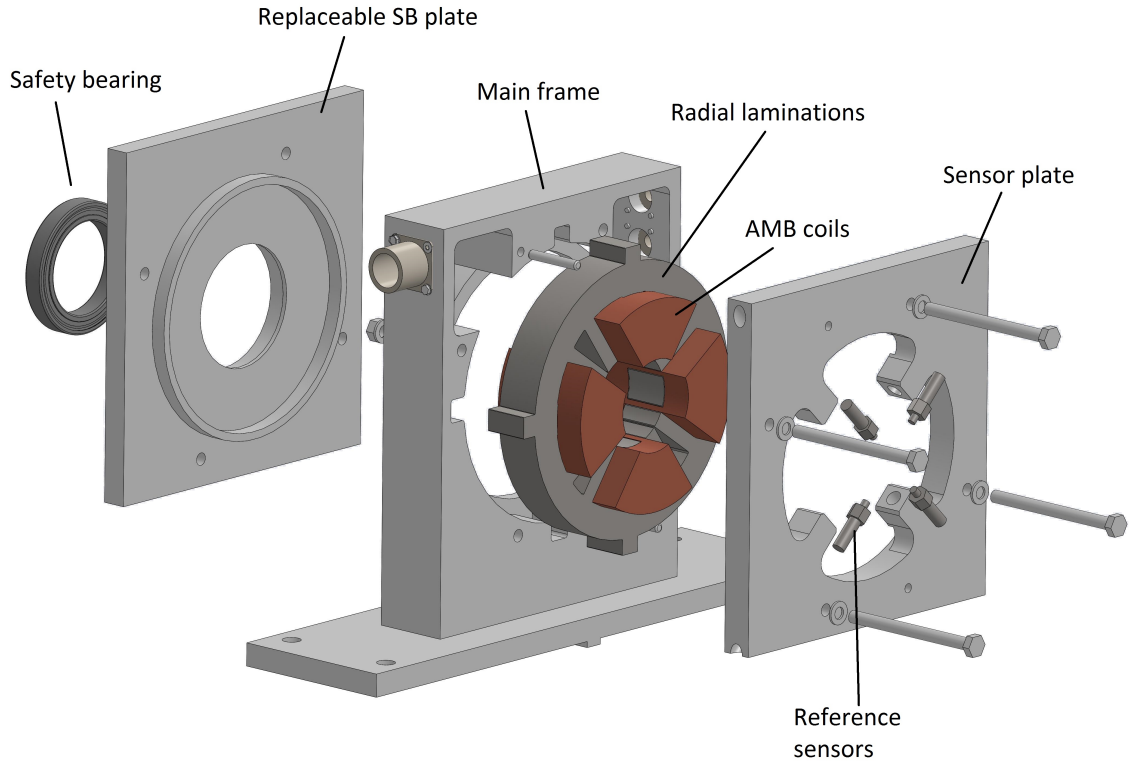

Figure 44. Main components of radial AMB module

The AMB stator is made using 0.35 mm electrical steel lamination sheets, the same material as the rotor radial laminations. Magnetic coils are wound around the poles in the laminations. The stator consists of four magnetic coils, which generate four magnetic main poles and eight smaller side poles. The rest of the module is magnetic steel, because the electromagnetic FEA indicated that there are no significant flux leakages in the module frame. In order to to have reliable positioning, the reference sensors are located right next to the AMB stator. On the other end is space for a safety bearing. The SB end plate is designed to be easily replaceable. In addition, safety bearing type and size can be changed. The conceptual module frame in Fig. 44 illustrates how different components

are designed to be in final construction.

During the design process, a number of different iterations for the magnetic insulation of the lamination stator were performed. One design iteration was to add non-magnetic end plates for the laminations. Another was to use segmented laminations. Both of these iterations used precision taps through laminations in order to lock the position to the module frame. This locking design was not practical in order to maintain the required accuracy. Therefore, the final construction of the preliminary design was to use full laminations with alignment grooves in the frame, as seen in Fig. 44.

3.4.3 Axial AMB module

In addition to the radial bearing module, also the axial bearing module is a combination of AMB and mechanical support. This supports by placing brass retainer rings into AMB stators to prevent contact between the axial disk and stators. Fig. 45 illustrates the conceptual design of the axial AMB module.

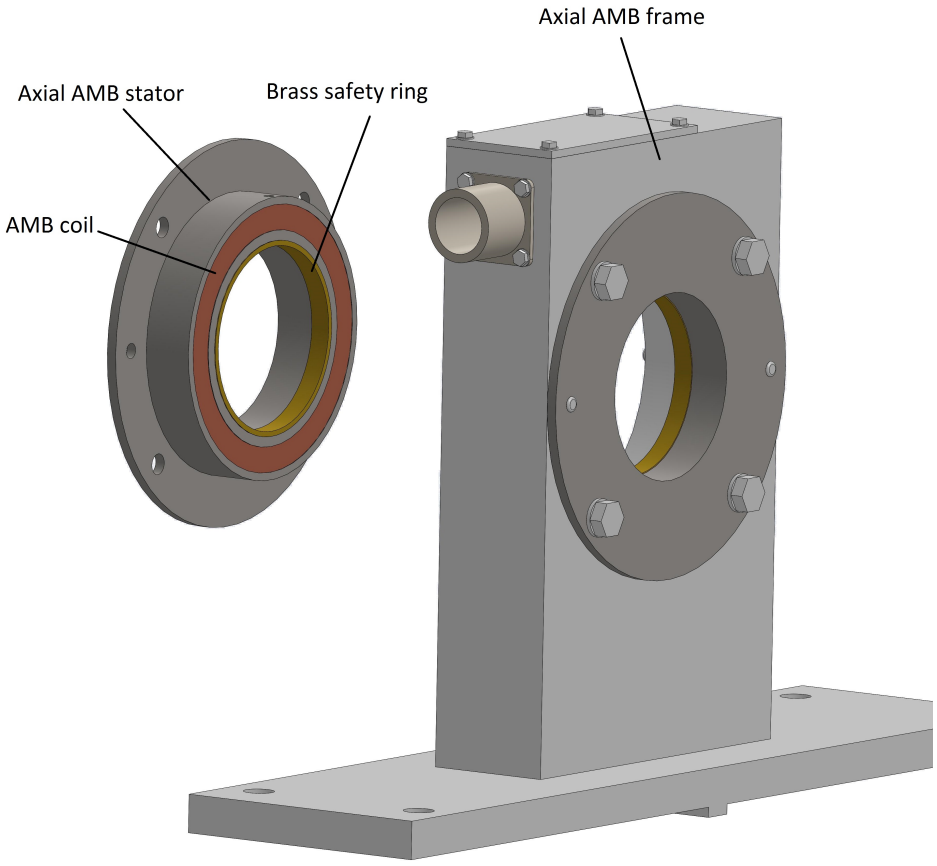

Figure 45. Main components of axial AMB module

In the case of axial AMB stators, the used material is solid magnetic steel S355. Actuator coils are wound around the stator pole. Therefore, the axial AMB stator consists of four magnetic poles. In order to prevent alternative flux paths and unwanted force vectors, the frame material cannot be magnetic steel. AISI 304 was originally chosen to be used, and the nut changed to aluminium, because it is also non-magnetic metal. Since there are no problems of thermal condition or expansion, aluminium was selected for its cheaper price. The sensor for the axial AMB is located on a separate frame at the other end of the rotor. The sensor surface is made of a separate aluminium disk that is fastened using threading.

3.4.4 Position sensors

AMBs require continuous feedback on the current position of the rotor. Therefore, eddy current sensors are used for positioning purposes for both radial and axial AMBs. Radial AMBs require two sensors in perpendicular configuration per module, but in order to perform differential measurements, total of four sensors are used. Radial sensors are located right after the coils and oriented to be between two coils. A magnetic measurement surface is required in order to optimize the performance of the eddy current sensor. Fig. 46 presents the voltage–distance curve for the CMSS 65-002-RM-12-5A eddy current sensor [28]. Considering sensor properties, AISI 4140 steel, also known as 42CrMo4, is selected as the sensor sleeve material for the radial sensors. The axial position sensor surface is placed at the end of the rotor as a small separate aluminium disk.

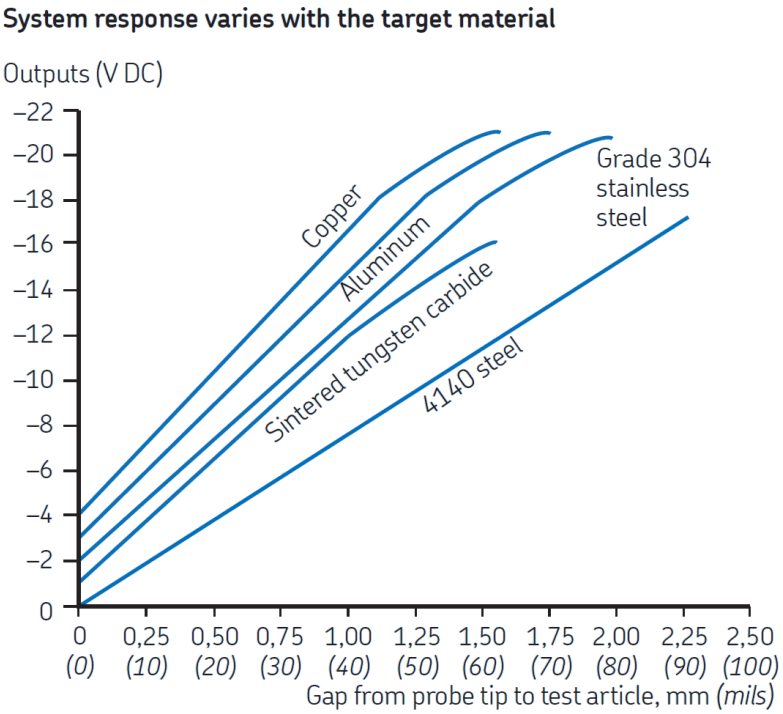

Figure 46. Eddy current sensor response curve [28]

In addition, temperature sensors are also designed to be added in the detailed design phase to the AMB stator to monitor temperature changes. The components most vulnerable to heat are the coils in the AMB stators. Depending on the quality grade of the copper wire used in the coils, the temperature cannot typically be higher than 120°C. An additional 4 cm free space is designed on the lamination sleeve to test different sensor technologies, such as induction and capacitive sensors.

3.5 Base plate and supporting frame

Due to the need for an easily reconfigurable module design, the base plate for the modules is designed to be able to ensure accurate positioning. Altogether, a 2.5 m long base plate includes T-slots for bolt fasteners to the modules and a middle rail for accurate positioning. Fig. 47 presents the structure of the base plate and the supporting frame as seen in ANSYS modal analysis tool. Structural steel S355 is used for all the parts. The frame is welded using hollow rectangular beam, and the base plate is bolted to the supporting frame.

Modal analysis is done to the base plate and the supporting frame in order to check if there

are any possible resonance frequencies with the rotor. The bolt connections between base plate plate and supporting frame are modelled as rigid connection, this illustrates the bolt preload. On the other hand, the contacts between the base plate and the supporting frame are frictional contacts using a friction coefficient of 0.2. The supporting frame is fixed from its bottom plates using the bolt connection surfaces as seen in Fig. 47. Rest of the connections in supporting frame are fixed, which illustrates the welding in the supporting frame. Direct solver is used. The total number of elements is 172 130 and number of nodes 619 805 using SOLID168, SOLID187, CONTA174 and TARGE170 element types.

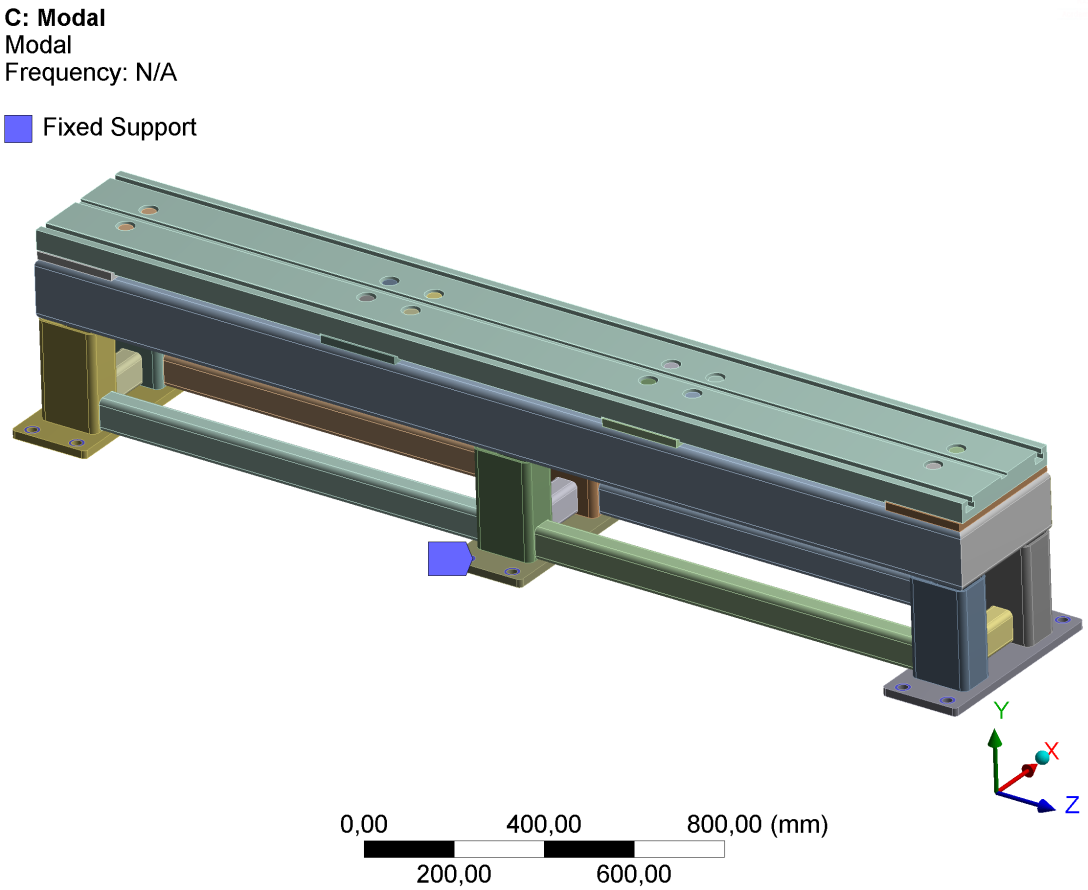

Figure 47. Base plate and supporting frame

The simulation is done with ANSYS using the frequency range from 100 Hz to 700 Hz. Table 6 presents all the frequencies, whereas Fig. 48 presents two closest modes with respect to the rotor eigenmodes, Fig. 48a is the closest base plate deformation modes according to the first eigenmode of the rotor. Respectively, Fig. 48b is the closest mode in the supporting frame according to the first eigenmode of the rotor. An automatic deformation scale is used.

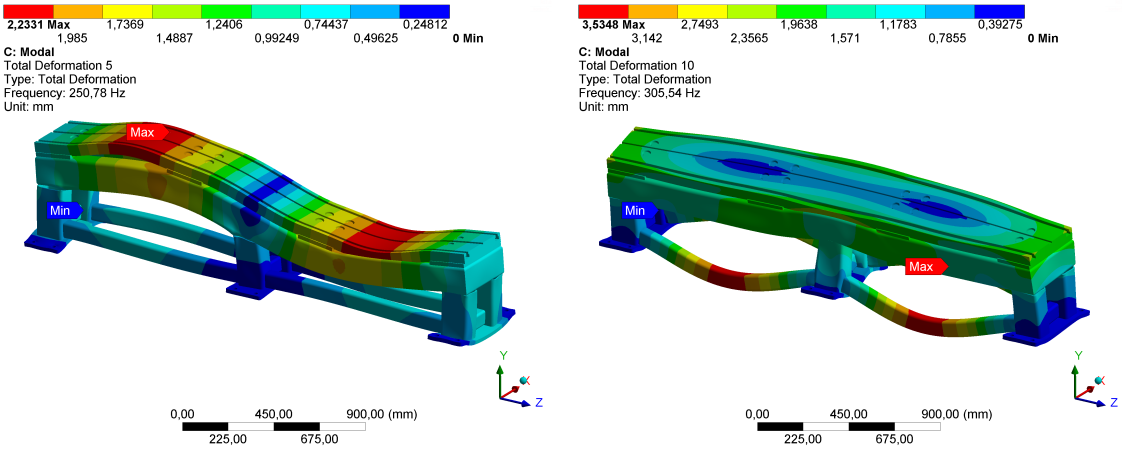

(a) Base plate deformation at 250.8 Hz (b) Supporting frame deformation at 305.5 Hz

Figure 48. Two close deformation modes according to the first rotor eigenfrequency

Table 6. Base plate and supporting frame eigenfrequencies

Mode	**Frequency [Hz]**				
1	101.9	10	305.5	19	465.1
2	141.2	11	334.0	20	471.5
3	168.2	12	334.4	21	537.7
4	197.9	13	337.6	22	539.1
5	250.8	14	340.4	23	544.0
6	289.7	15	361.3	24	610.4
7	293.2	16	369.7	25	618.7
8	293.5	17	415.3	26	621.5
9	294.7	18	426.2	27	631.4

4 REVIEW OF THE DEVELOPMENT IN THE RECONFIGURABLE TEST RIG PROJECT

The design and analysis of the test rig presented in this thesis concentrates on the Configuration I. This particular configuration is only one of the total of three different test rig configurations. Schematic of the project is presented in Fig. 49. The arrows presents relations between different configurations and tasks. Also, tasks will be performed in the order as shown in Fig. 49.

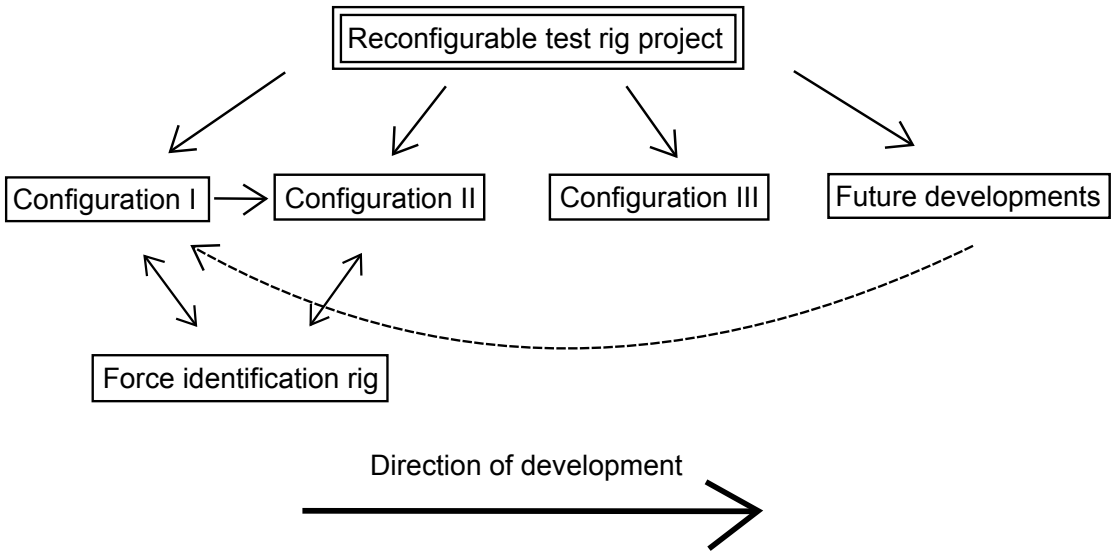

Figure 49. Schematic of the Reconfigurable test rig project

One of the main purpose of the Configuration I is to test the accuracy of modular design and positioning. This information can be used for designing the Configuration II, which is going to be very similar to the first one. Main role is also with the Force identification rig. With this device the identification of the magnetic actuators can be studied and verified. This essential information is needed in order to make an accurate controlling system model that can be verified afterwards in the real environment.

Configuration III, a Bearingless motor, is quite different concept than the first two. In this configuration the radial AMB module and the induction motor module are integrated into one module providing both motoring and suspension. All the configurations are designed to operate at 30 000 rpm. The rest of the design specification are similar to the Configuration I excluding the major differences caused by different kind of topology of

the actuators. In addition, LUT Voima has developed a calibration rig for calibrating the reference sensors and mounting them in the sensor plate.

In addition, the Reconfigurable test rig project offers further capabilities to carry out studies according to safety bearing technology by making drop down tests, and to test bearing mounting methods, such as an elastic bearing mounting. Also, air and fluid film bearings can be studied. One of the reasons of designing longer sleeves than needed to the Configuration I rotor is to enable studies of different sensor technologies, and also to make it possible to study hydrodynamic fluid film bearings.

4.1 Force identification rig

The Force identification rig is designed to provide a component identification. Fig. 50 illustrates the concept design of this rig. The basic idea in the rig is to perform force measurement by means of varying the air gap of the bearing. The force measurement is done using six axis force sensors. A radial AMB module is in the middle of the rig providing the magnetic force to the rotor laminations, which are connected to the dummy shaft. This shaft transfers the load to the force sensors. The reference sensors of the radial AMB module can be used to identify the accurate position of the dummy shaft, and therefore the air gap. There will be differences in the position of the linear stages and the reference sensors when the magnetic force is applied. This is caused by the relatively low stiffness of the strain gauge type sensors. Therefore, the sensors cause minor flexible movement. Of course, this can be compensated using a feedback loop in the stage control system.

The maximum load capacity of one sensor is 1 900 N at one end of the rig. Therefore, besides the radial AMBs, also the conical AMBs can be measured. The variation to the air gap is done using motorized linear stages connected perpendicularly as seen in Fig. 50. Of course, using two stages at the one end of the rig enables only two dimensional force measurement. Still, the axial force measurement can be achieved with this type of rig. One method to implement the proper axial force measurement capability is to add one more stage which would control the axial position of the AMB module as seen in the middle of the rig.

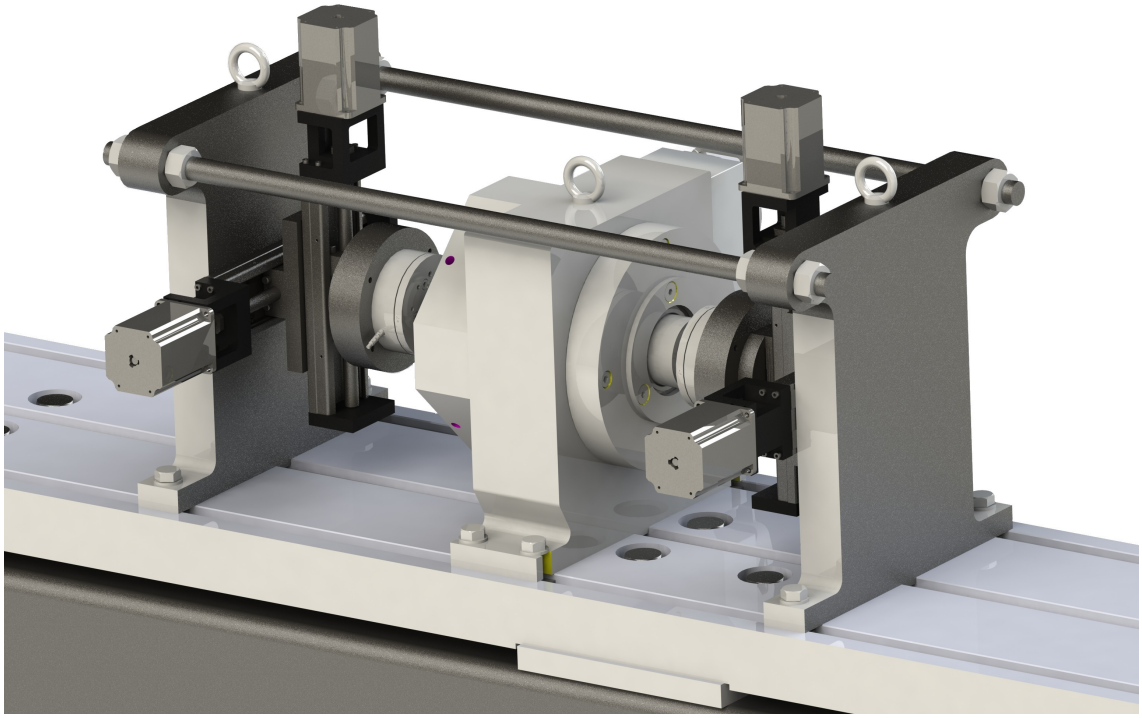

Figure 50. Force identification rig concept design

Even though the concept design looks relatively simple, the force and the bending moment calculation required time to optimize the size of the stages. Depending on the size of the stage the stepper motor has to be able to provide torque high enough. Also, to optimize the functionality of the rig, a synchronous motor control is required. In order to make the structure rigid enough, the overhang supporting rods are added to the design. Still, issues regarding accuracy may occur due to the tolerances used and the dynamic behaviour of the stages and the sensors.

4.2 Configuration II: Conical AMBs

The Conical AMB design is very similar to the detailed design of the Configuration I. Fig. 51 presents the detailed design of the Configuration II provided by LUT Voima. The only difference is that radial AMB stators are changed to conical AMB stators. Respectively, rotor laminations are also changed to the conical shaped laminations with the conical angle of 6.4°. Therefore, these two conical AMB modules seen in Fig. 51 will provide both radial and axial support. The radial and the axial forces are calculated to be practically the same as in the Configuration I, since the rotor geometry and weight is almost the same as in the Configuration I rotor.

The conical AMB stator laminations have also an E-core configuration as in the Configuration I AMB stator laminations introduced in section 3.4.2. The main difference is that the conical AMB stators are segmented and permanent magnets are placed between the side poles. In order to prevent the flux leakage according to electrical FEA in magnetic steel module frame, the material is changed to aluminium.

One iterated safety configuration was to use two single row angular contact bearings in X-arrangement on the one end of the rotor and a one deep groove ball bearing on the other end of the rotor. Therefore both radial and axial support would have been possible using rolling element bearings. Unfortunately, the rotor and the conical AMB module dimensions did not allow to use these kind of safety bearings. This configuration would have required additional shoulders on both sides of the angular contact bearings in order to provide also the axial support. Considering modular structure, installing the conical AMB module from the other end of the rotor was not possible. Therefore, two deep groove ball bearings are used for radial support like in the Configuration I and the axial AMB disk and the axial AMB module are added to the design only to provide mechanical support in axial direction.

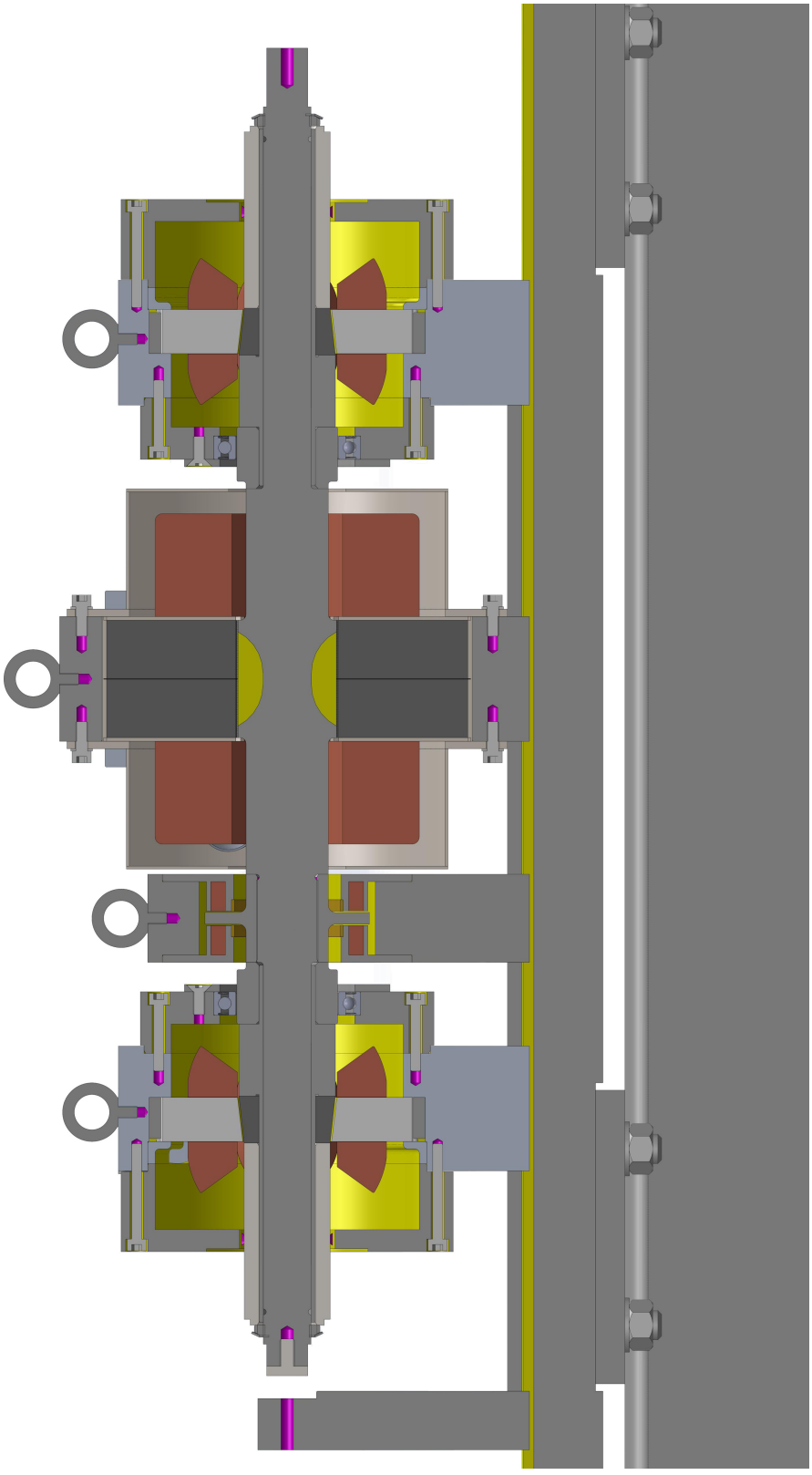

Figure 51. Cross section of detailed Configuration II design with conical AMBs

4.3 Configuration III: Bearingless motor

Configuration III includes a bearingless motor, which means that the radial AMBs and the permanent magnet synchronous motor windings are combined into one stator, therefore providing both motoring and suspension. The magnetic levitation works using the rotor lamination as in the previous configurations. A number of permanent magnets with relatively high remanence of one tesla, are added inside the laminations. These permanent magnets provide four fixed magnetic poles inside the rotor laminations. By means of two different magnetic fields acting, the levitation and the torque can be applied to the rotor. Therefore, the rotor include characteristics of a rotor of a permanent magnet machine. Fig. 52 illustrates the concept design of the rotor of the Bearingless motor with three actuators.

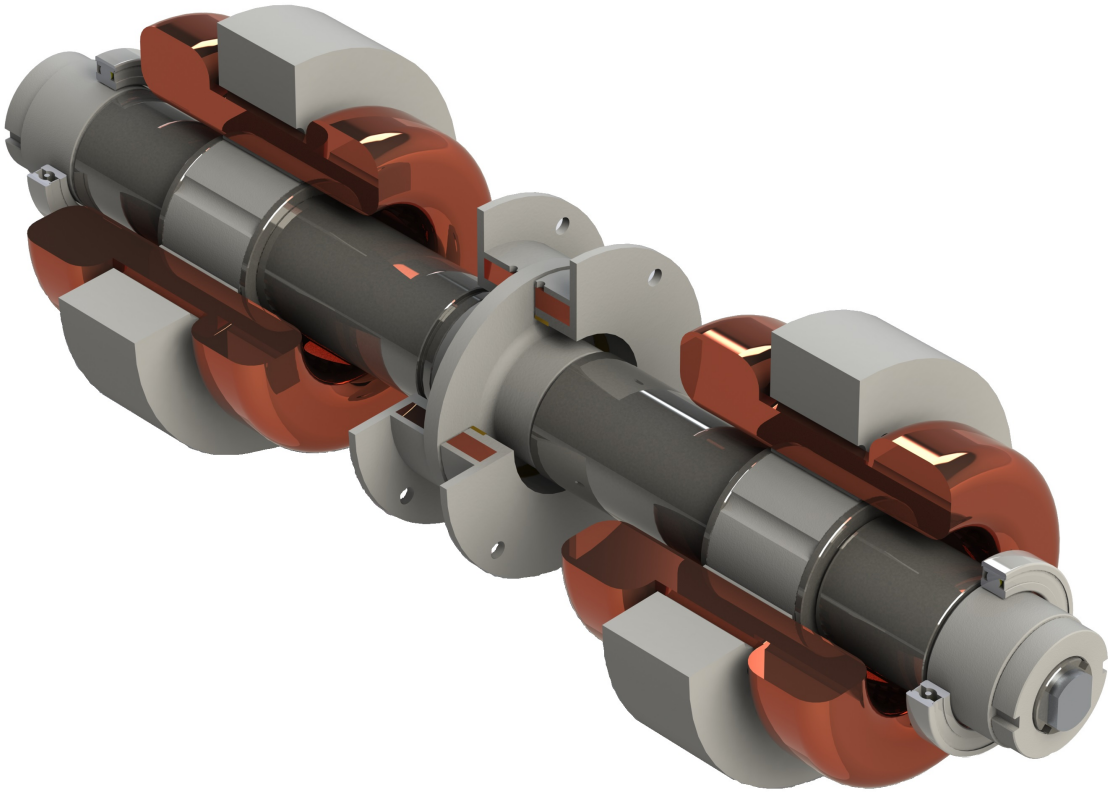

Figure 52. Concept design of Bearingless motor

The design iteration process of the rotor lamination geometry has taken multiple iterations. This special lamination geometry with OD of 70 mm is presented in Fig. 53. There are total of 20 gaps for the permanent magnets which are glued to the lamination stack. In addition, four gaps are added to the outer surface of the lamination sheet. These

gaps provide additional benefits to the flux density between the magnetic poles.

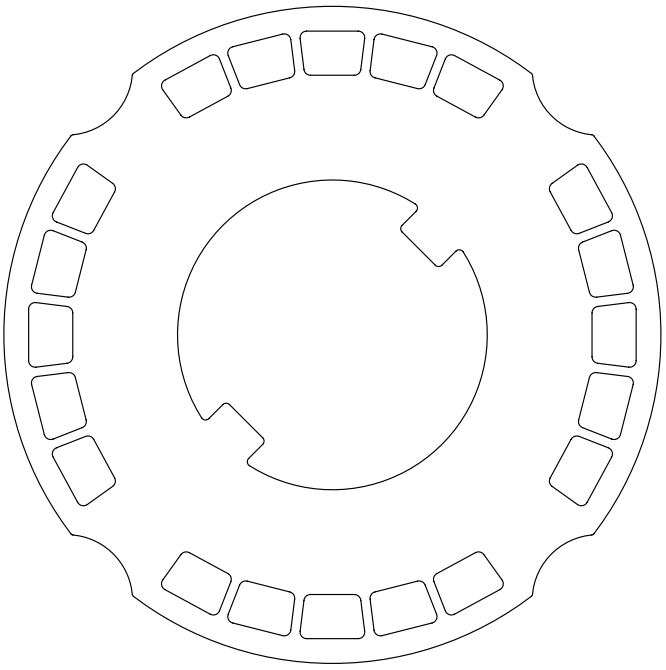

Figure 53. Lamination sheet geometry of the rotor of Bearingless motor

Since the permanent magnet rotor provides also torque a rigid connection is required between the lamination stack and the shaft. A shrink fit connection yield very high stresses compromising the mechanical durability of the lamination stack. Therefore, a wedge is needed to ensure the connection between the lamination stack and the shaft. A separate wedge is practical, but the gap for the wedge in the lamination sheet yield again very high stresses. Therefore, the wedge is integrated to the lamination geometry. Now, the stresses are acceptable. The second wedge is added in order to make the geometry symmetrical for electrical reasons. On the other hand, there is a drawback. The shaft needs to have long grooves for the wedges beginning from the end of the shaft causing additional phenomena in the rotordynamic behaviour.

5 DISCUSSION

5.1 Design iteration process

Due to the need of changeable lamination sleeve assemblies, the shrink fit between the shaft and lamination sleeve is minor. Therefore, spinner nuts are added to hold the lamination sleeve components together by the axial force generated by the high tightening moment of the spinner nuts. The selected values for the interference for lamination tubing–laminations contact is higher than needed, but idea is to take into account possible variations in fabrication tolerances. In addition, no surface tolerances, surface qualities and installation tolerances have been taken into account.

Due to the fact that all materials used in the rotor have similar mechanical properties, thermal considerations were not needed to take into account, because the thermal expansion in the interference fits will be only minor. In addition, the thermal expansion coefficient is practically the same with all the materials used in the rotor. Considering the Conical AMB test rig introduced in section 4.2 the thermal expansion in axial direction will have impact to the performance of the conical AMBs. An average of 50°C temperature change between the rotor and the base plate will cause 200 μm expansion in axial direction.

The initial design for fastening the modules to the base plate using T-slots proved to be the final method for fastening. On the other hand, the T-slots are not quite accurate, therefore the third rail was added to the middle used for accurate module positioning. The base plate was also lengthened up to 2.5 m in order to test longer rotors or even connect two AMB systems in series.

The radial AMB module design took the most iteration steps. In order to increase practicality and usability, the position of the reference sensors was redesigned multiple times. Also, the supporting structure for the radial laminations was iterated several times.

The position of the axial AMB disk on the rotor does not cause any problems when assembling the device, since the inner diameter of the axial AMB stator half is greater than the outer diameter of the rotor part for the induction motor module. Still, the axial AMB module can be assembled just when assembling the whole test rig configuration. The rest of the modules can be used preassembled instead.

5.2 Rotor finite element analyses

The operational speed of the rotor is specified to be 30 000 rpm. In simulations the value of 34 000 rpm was used to apply 13 % overspeed. The lamination sleeve shrink fit was iterated to be 15 μm. This interference yields high enough radial stress to maintain the connection between sleeve components. Axial fastening forces of the spinner nuts and the threading of the axial AMB disk were added to the ANSYS model. AMB forces were also added to the rotor finite element model to maximize stresses of the electromagnetic components. A safety factor of 1.5 was used. On the other hand, these additional loads have only a minor impact considering the high centrifugal forces. No thermal loads were taken into account, since the thermal expansion coefficient is the same for all materials used in the sleeve construction. On the other hand, some approximations were calculated concerning axial thermal expansion. If the axial AMB disk is assumed to be a reference point, then the maximum displacement at further radial AMB is 0.86 mm at an 80°C temperature change.

Analytical results were obtained using MATLAB script introduced in Appendix 2. There are some differences between FEM and analytical modelling. For instance, the analytical sleeve model does not take into account the axial force caused by spinner nuts and the axial AMB disk threading. Therefore, the axial force is neglected in the equivalent stress of the components. Also, the analytical MATLAB model does not take into account the shaft–lamination tubing contact. Therefore, the FEA stresses can be higher, since there are three layers of different materials. The analytical model of the axial disk is assumed to be a plain disk without supporting sleeves on both ends of the disk. Therefore, some differences in stresses because of the axial tightening force is neglected and also the axial AMB force is neglected. A 3D model of axial AMB disk distributes the stresses more to the sleeves than compared to analytical results. The stresses of the rotor are minor, even at the slits.

Comparing radial stresses between models indicates that the FEM results are higher, since the finite element model includes the shaft which creates additional radial stress by reducing displacement at the inner surface of the lamination tubing. Also, tangential stresses are a bit higher in the finite element model. A comparison of simulation results of the lamination sleeve indicates that current stresses are far from the maximum allowed stresses. Therefore, even results vary between FEM and analytical model; because of the differences in the simulated case, they are still well within the range of material maximum stresses. In general, the comparison between these two modelling methods indicated that all the stress components behave similarly. The main stresses in the lamination sleeve

structure is about 150 MPa using both analytical and finite element approach. These stresses yields the safety factor of 2.37 for this part of the rotor.

Since there is no shrink fit in the axial AMB disk connection, maximum radial stress radially affects in the middle of the disk. There is a major difference in the tangential stresses of the axial AMB disk. This can be explained by the difference of the used geometry. The analytical model is made for a plain disk, whereas the finite element model includes a supporting sleeve at both end of the disk with 5 mm roundings. These supporting sleeves and roundings distribute the tangential stress so well that a 29% reduction is seen between the two models, which explains the major difference in the tangential stress. Also, the difference in stresses is partially caused by differences in simulated geometry and the presence of the axial force in the finite element model. The highest stresses are in the axial disk, since its OD is the highest. In the finite element model, the spinner nuts cause local peaks in the results, but this is only because the unoptimized geometry used in the model. The maximum stress of the axial AMB disk is the equivalent stress with approximately 260 MPa. This yields a safety factor of 1.37 for the axial AMB disk.

5.3 Modal analyses

The eigenmodes of the rotor were studied in order to find out possible eigenfrequencies close or below the nominal operational speed. Due to the multiple part structure and rechangeability of the lamination sleeve, a rough estimation is done in order to approximate the behaviour of the lamination sleeve by reducing the normal elastic modules of the used materials while using normal densities and Poisson's ratios. In general, comparing the results of the beam element model and the solid element model, both have relatively close results.

When analysing the measured data the three first bending eigenfrequencies can be easily discovered. On the other hand, there seems to be easily noticeable secondary dampened bending eigenfrequencies for the first two primary bending eigenfrequencies. The measurement was done only once, if the orientation of the rotor would have changed and multiple measurements done the results could have been more accurate. It is difficult to say are these presented results accurate or not. While performing the measurement the impact hammer was placed approximately in a position where the node point of the first eigenmode appeared, approximately one forth of the rotor length from other end of the rotor.

By comparing the results, the twenty percent approximation was closest to the measured data. Typically, the second simulated eigenfrequency is more inaccurate than the first one. This same tendency was seen in the results. According to a study by Lantto [27] the impact of the laminations over the shaft was approximated by using zero pascals as the elastic modulus for the laminations and impellers. The beam and solid element models used in this thesis did not work correctly when using exactly zero elastic modulus. Therefore, the case of one percent elasticity was used to study the negligible elasticity of the laminations sleeve parts.

The main difference between the beam and solid element models is that the solid element model uses frictional contacts whereas the individual parts are defined as layers with different material properties in the beam element model. Axial forces caused by tightening torque of the spinner nuts were not included in the models. Also, the forces caused by shrink fits were not modelled because low stiffness of the lamination sleeve parts and high loads would have caused unrealistically large deformations in the solid element model. More importantly, this kind of shrink fit modelling approach is not possible in the beam element model. The measured data and FEA model analysis results comparison shown in section 3.3.6 reveal that the lamination sleeves contribution to the stiffness of the rotor is more challenging to model than what was initially expected based on the previously referred study. Nevertheless, twenty percent elastic modulus of the lamination sleeve parts in the FEA models resulted to acceptable bending eigenfrequencies.

The rotor eigenfrequency measurement was performed once in one particular orientation of the rotor. Furthermore, the disturbance impact point was approximately in the same location as the node point of the first eigenmode. This measurement factor partially contributed to measured lower than expected amplitude for the first eigenmode.

A modal analysis was performed also for the base plate and the supporting frame. The purpose of this study was to check if there is a possible common resonance frequency in both the rotor and the frame. Results indicate that there is a possible resonance point close to the first eigenmode of the rotor according to the measured rotor data. The first eigenfrequency of the rotor is 259.4 Hz, whereas the closest base plate eigenfrequency is at 250.8 Hz. However, the mass of the modules was not taken into account. In case if there is need to have additional damping to the base plate, the hollow rectangular beams of the supporting structure can be filled with sand and elastic material such as rubber sheets can be placed between the base plate and the supporting structure.

6 CONCLUSIONS

In this thesis, the conceptual design and analysis of a reconfigurable AMB test rig was done. The designed machinery is the first configuration of a total of three setups of the AMB study and verification project. The main focus was an designing a high speed rotor with AMB support. An iterative rotor design method was documented according to the main points, such as specification definition, selection of the material, providing concept design and performing a strength analysis. Due to the fact that the design is conceptual, no rotordynamics studies, such as a Campbell diagram, were performed since the bearing technology is designed and verified by the professionals of the LUT Laboratory of Control Engineering and Digital Systems. Mechanical bearing support modelling in the rotordynamics study is possible in ANSYS, but modelling the digital control system for AMBs is probably not possible in this environment. On the other hand, free-free modes of the designed rotor was studied.

A detailed analysis of the high speed rotor was performed in two viewpoints. Preliminary results were obtained by means of analytical modelling. These results were compared to the results of accurate 3D model. As expected, some differences were found. However, both methods were proved usable in designing a high speed rotor. This approach pointed out both benefits and limitations in simplified analytical modeling. The interference fits in the sleeve structures, which is one of the most critical parts of the rotor design, was carried out using analytical modelling. Due to the fact that the shrink fit in the sleeve structure is small, the variation of the maximum stresses is also small.

As mentioned, this thesis covers only the concept design of the test rig. Some additional issues that are required in detailed design are the possible problems of fabricating very accurate tolerances and surface qualities needed to ensure accurate positioning of the modules and electromagnetic actuators. There may always be problems with thermal expansion, since the rotor is light when compared to the modules and large stators can dissipate generated heat more effectively than the rotor. On the other hand, the IM stator is required to have a blower for air cooling which can also be used to cool the rotor. This requirement is for fully loaded 10 kW induction motor. In practice concidering the test environment, the motor with only a fraction of a full load will not have heating problems. The concept design of module structures includes material selections and essential components for AMBs. Free space in the modules was increased in later design phases for enabling integrated temperature sensors, space cabling and power connectors.

An eigenmode study was performed to the fabricated rotor. This study gave valuable

information that was used to identify the rotor eigenfrequency model. Differences between the beam and solid element models used to study the eigenfrequencies were discussed. The impact of the stiffness used in the modelled lamination sleeves was studied and documented. Also, the accuracy of the physical measurement was discussed. According to the measured rotor eigenfrequencies and simulated base plate eigenfrequencies there is one possible resonance frequency.

Future developments in the reconfigurable test rig project include implementing the other two configurations. The second configuration will comprise conical AMBs and the third design will include a bearingless motor, where radial AMBs include also torque winding, and rotor laminations include characteristics of a permanent magnet rotor. Also, under investigation is a design of an identification rig for radial AMBs, with which the functionality of AMBs can be studied and verified.

In addition, the test rig project offers further capabilities to carry out studies according to safety bearing technology by making drop down tests, and to test bearing mounting methods, such as an elastic bearing mounting. Also, air or fluid film bearings can be studied. One reason to design a longer rotor than needed in the first configuration of the project was to enable studies of different sensor technology, and also to make it possible to study hydrodynamic fluid film bearings.

REFERENCES

[1] RoMaDyC Center for Rotating Machinery Dynamics and Control. Web page. http://academic.csuohio.edu/romadyc/. Visited: 3.4.2014.

[2] T.R. Grochmal and C.P. Forbrich. Self Bearing Motor. Web page. http://www.ancl.ualberta.ca/en/Research/Projects/SelfBearingMotor.aspx. Visited: 21.7.2014.

[3] S.E. Mushi, Zongli Lin, and P.E. Allaire. Design, Construction, and Modeling of a Flexible Rotor Active Magnetic Bearing Test Rig. *IEEE/ASME Transactions on Mechatronics*, 17(6):1170–1182, Dec 2012.

[4] C.J.G. Ranft. *Mechanical Design and Manufacturing of a High Speed Induction Machine Rotor*. North-West University, Potchefstroom Campus, 2010.

[5] H. Bleuler, G. Schweitzer, and E.H. Maslen. *Magnetic Bearings: Theory, Design, and Application to Rotating Machinery*. Springer, 2009.

[6] E.E. Swanson, E.H. Maslen, G. Li, and C.H. Cloud. Rotordynamic Design Audits of AMB Supported Machinery. *Proceedings of the Thirty-Seventh Turbomachinery Symposium*, 2008.

[7] F. Lösch. *Identification and Automated Controller Design for Active Magnetic Bearing Systems*. Swiss Federal Institute of Technology, ETH Zürich, 2002.

[8] S.Y. Yoon. *Surge Control of Active Magnetic Bearing Suspended Centrifugal Compressors*. University of Virginia School of Engineering and Applied Science, 2011.

[9] A. Kärkkäinen. *Dynamic Simulations of Rotors During Drop on Retainer Bearings*. Lappeenrannan Teknillinen Yliopisto, 2007.

[10] L. Hawkins, A. Filatov, S. Imani, and D. Prosser. Test Results and Analytical Predictions for Rotor Drop Testing of an Active Magnetic Bearing Expander/Generator. *Journal of Engineering for Gas Turbines and Power*, 129:pp. 522–529, 2007.

[11] I.S. Cade, M.N. Sahinkaya, C.R. Burrow, and P.S. Keogh. On the Use of Actively Controlled Auxiliary Bearings in Magnetic Bearing Systems. *Journal of Engineering for Gas Turbines and Power*, 131(2):pp. 1–10, 2008.

[12] R.W. Bruce. *Handbook of Lubrication and Tribology, Volume II: Theory and Design*. CRC Press, 2012.

[13] S.R. Schmid, B.J. Hamrock, and B.O. Jacobson. *Fundamentals of Machine Elements*. CRC Press, 2014.

[14] W.H. Dornfeld. *Thick-Walled Cylinders and Press Fits*. Cource handout. ME311 Machine Design. Fairfield University School of Engineering, 2004.

[15] Y. Zhu. *Thick-Walled Cylinders*. Cource handout. MAE 316 Strength of Mechanical Components. North Carolina State University Department of Mechanical & Aerospace Engineering, 2013.

[16] R. Larsonneur. *Design and Control of Active Magnetic Bearing Systems for High Speed Rotation*. Swiss Federal Institute of Technology, 1990.

[17] Engineers Edge. Fastener Screw Torque Clamp Force Design Calculator. Web page. http://www.engineersedge.com/torque.htm. Visited: 4.6.2014.

[18] J. Karhula. *Koneenosien suunnittelu*. Cource handout. BK65A0100 Koneenosien suunnittelu. Lappeenrannan teknillinen yliopisto, 2009.

[19] PENCOM. Screw Design Guide. Web page. http://www.pencomsf.com/screws-categories/screw-design-guide/. Visited: 6.6.2014.

[20] SKF. HYDROCAM bolt tensioners. PDF document. http://www.skf.com/binary/12-124616/PUB_MT-P2_10255_EN.pdf. Visited: 11.6.2014.

[21] W.J. Chen and E.J. Gunter. *Introduction to Dynamics of Rotor-Bearing Systems*. Trafford Publishing, 2005.

[22] ANSYS, Inc. ANSYS Mechanical APDL Contact Technology Guide. PDF document. http://148.204.81.206/Ansys/150/ANSYS%20Mechanical%20APDL%20Contact%20Technology%20Guide.pdf. Visited: 10.7.2014.

[23] Surahammars Bruk. Typical Data for SURA® M270-35A . PDF document. http://www.sura.se/Sura/hp_products.nsf/vOpendocument/03A8B2433FAE16C4C1256AA8002280E6/$FILE/270-35.pdf?OpenElement. Visited: 7.4.2014.

[24] STEELSS Special Steel Suppliers. Data Table for Carbon Steel. Web page. http://www.steelss.com/Carbon-steel/. Visited: 12.6.2014.

[25] Ruukki. Hot-rolled Steel Plates, Sheets and Coils. PDF document. http://www.ruukki.com/~/media/Files/Steel-products/Hot-rolled-standard-steels/Ruukki-Hot-rolled-steels-Standard-steel-grades-comparison-designation-and-codes1.pdf. Visited: 12.6.2014.

[26] Ovako. CROMAX 42CrMo4. PDF document. http://www.pencomsf.com/screws-categories/screw-design-guide/. Visited: 12.6.2014.

[27] E. Lantto. *Finite Element Model for Elastic Rotating Shaft*. Acta Polytechnica Scandinavica, Electrical Engineering Series, 1997.

[28] SKF. Eddy Probe Systems Catalog. PDF document. http://www.skf.com/binary/83-48660/Eddy-Probe-Systems.pdf. Visited: 2.7.2014.

Appendix 1. Fulfilled design specifications

Table A1.1. Test rig rotor specifications

Rotor	
Operational speed	30 000 rpm
Rotor OD	112 mm
Surface velocity	176 m/s
Shaft length	897.5 mm
Mass	17.7 kg
Rotor OD	67 mm
Rotor length	80 mm
Rotor slits	Curved slits 14 pcs.
Slit length	64 mm
Slit width	2.5 mm
Slit depth	17 mm
Radial AMB rotor lamination OD	58.5 mm
Radial lamination stack length	32 mm
Axial AMB disk OD	112 mm
Axial AMB disk length	8 mm
Axial AMB disk	Solid magnetic steel disk

(continues)

Appendix 1. (continued)

Table A1.2. Test rig module specifications

Induction motor	
IM power	10 kW
Stator inner diameter	70 mm
Stator outer diameter	252 mm
Stator stack length	80 mm
Stator slots	12 pcs.
IM stator air gap	1.5 mm
Bearings	
Radial stator inner diameter	60.5 mm
Radial stator outer diameter	158 mm
Radial stator stack length	30 mm
Radial AMB stator	E-core lamination, 12 poles
Radial AMB force	282 N
Radial AMB air gap	1.0 mm
Radial SB air gap	750 μm
Radial SBs	61912 (60-85-13)
Axial AMB stator	Solid magnetic steel stators
Axial AMB force	127 N
Axial AMB air gap	1.0 mm
Axial SB air gap	700 μm
Axial SBs	Brass retainer rings
Base plate and frame structure	
Base plate length	2 500 mm
Base plate width	300 mm
Rotor height from base plate	160 mm
Base plate height from ground	505 mm

Appendix 2. Rotor-sleeve connection modelling script

```
% Rene Larsonneur - PhD "Design and control of active magnetic bearing
% systems for high speed rotation" pp. 11-31, pp. 146,147.
% Radial, tangential and von Mises stress in two shrink-fitted rings

% Original MATLAB script from Cornilius Ranft. Dissertation of "Mechanical
% design and manufacturing of a high speed induction machine rotor"

% Modified by: Eerik Sikanen
% Date: 10.6.2014

clear all, close all, clc
tic

% Initial values ############################################################
Nsim = 250;
rpm_min = 0;
rpm_max = 34000;

% Inner ring
ri1 = 32.5e-3/2;
ro1 = 38.5e-3/2;

% Outer ring
ri2 = 38.5e-3/2;
ro2 = 58e-3/2;

delta_r = 15e-6; % radial interference
delta_T = 0;
% Initial values ############################################################

% Material Data #############################################################
% AMB tubing
rho1 = 7865; % (kg/m^3)
E1 = 200e9; % (N/m^2)
v1 = 0.285; % Poisson's ratio
alpha1 = 16.5e-6; % (m/m-C) Coef. of therm. expansion

% Sensor sleeve
rho2 = 7865; % (kg/m^3)
E2 = 200e9; % (N/m^2)
v2 = 0.285; % Poisson's ratio
alpha2 = 16.5e-6; % (m/m-c) Coef. of therm. expansion

% % Lamination sleeve
% rho2 = 7650; % (kg/m^3)
% E2 = 185e9; % (N/m^2)
```

(continues)

Appendix 2. (continued)

```
% v2 = 0.28; % Poisson's ratio
% alpha2 = 16.5e-6; % (m/m-c) Coef. of therm. expansion
% Material Geometry ######################################################

% Taking account temperature change and interference fit
ro1 = ro1 + alpha1*delta_T*(ro1);
ri2 = ri2 - delta_r + alpha2*delta_T*(ri2);
ro2 = ro2 + alpha2*delta_T*(ro2);

r = linspace(ri1+50e-6,ro2,Nsim);
rpm = linspace(rpm_min,rpm_max,Nsim);
Ohmega = rpm/60*2*pi;
u = zeros(Nsim,1);
epsilon_r = zeros(Nsim,1);
epsilon_t = zeros(Nsim,1);
sigma_ref_max = zeros(Nsim,1);
A = [ 0 1 0 0;
E1*(1+v1)/(1-v1^2) -E1*(1-v1)/((1-v1^2)*ro1^2) -E2*(1+v2)/(1-v2^2) E2*...
(1-v2)/((1-v2^2)*ri2^2);
ro1 1/ro1 -ri2 -1/ri2;
0 0 (1+v2) -(1-v2)/ro2^2];
x = zeros(4,1);
A_inv = inv(A);

for cntr1 = 1:Nsim % Speed loop

    F = [ 0;
        Ohmega(cntr1)^2/8*(rho1*(v1+3)*ro1^2 - rho2*(v2+3)*ri2^2);
        Ohmega(cntr1)^2/8*(rho1*(1-v1^2)*ro1^3/E1 - rho2*(1-v2^2)*ri2^3/...
        E2) - ro1 + ri2;
        rho2*Ohmega(cntr1)^2*(1-v2^2)*(v2+3)*ro2^2/8/E2];
    x = A_inv*F;

    for cntr2 = 1:Nsim % Radius loop

        if r(cntr2) <= ro1
            u(cntr2) = x(1)*r(cntr2) + x(2)/r(cntr2) - (1-v1^2)/8/E1*...
                rho1*r(cntr2)^3*Ohmega(cntr1)^2;
            epsilon_r(cntr2) = x(1) - x(2)/r(cntr2)^2 - 3*(1-v1^2)/8/E1*...
                rho1*r(cntr2)^2*Ohmega(cntr1)^2;
            epsilon_t(cntr2) = x(1) + x(2)/r(cntr2)^2 - (1-v1^2)/8/E1*...
                rho1*r(cntr2)^2*Ohmega(cntr1)^2;
            sigma_r(cntr1,cntr2) = E1/(1-v1^2)*(epsilon_r(cntr2) + v1*...
                epsilon_t(cntr2));
            sigma_t(cntr1,cntr2) = E1*epsilon_t(cntr2) + v1*...
                sigma_r(cntr1,cntr2);
```

(continues)

Appendix 2. (continued)

```
93
94          else
95              u(cntr2) = x(3)*r(cntr2) + x(4)/r(cntr2) - (1-v2^2)/8/E2*...
96                  rho1*r(cntr2)^3*Ohmega(cntr1)^2;
97              epsilon_r(cntr2) = x(3) - x(4)/r(cntr2)^2 - 3*(1-v2^2)/8/E2*...
98              rho2*r(cntr2)^2*Ohmega(cntr1)^2;
99              epsilon_t(cntr2) = x(3) + x(4)/r(cntr2)^2 - (1-v2^2)/8/E2*...
100                 rho2*r(cntr2)^2*Ohmega(cntr1)^2;
101             sigma_r(cntr1,cntr2) = E2/(1-v2^2)*(epsilon_r(cntr2) + v2*...
102                 epsilon_t(cntr2));
103             sigma_t(cntr1,cntr2) = E2*epsilon_t(cntr2) + v2*...
104                 sigma_r(cntr1,cntr2);
105         end
106
107         sigma_tresca(cntr1,cntr2) = max([abs(sigma_t(cntr1,cntr2) - ...
108         sigma_r(cntr1,cntr2)),abs(sigma_r(cntr1,cntr2))
109         abs(sigma_t(cntr1,cntr2))]);
110         sigma_von_mises(cntr1,cntr2) = sqrt(sigma_r(cntr1,cntr2)^2 - ...
111             sigma_t(cntr1,cntr2)*sigma_r(cntr1,cntr2) + ...
112             sigma_t(cntr1,cntr2)^2);
113     end
114 end
115 toc
116
117 % Plotting highest speed results
118 rpm_plot = Nsim;
119
120 subplot(3,1,1)
121 [ax4,h3] = suplabel('AMB sleeve - sensor surface contact', 't');
122 set(h3,'FontSize',20)
123 set(0,'DefaultAxesFontSize', 14)
124 set(0,'DefaultTextFontSize', 14)
125 plot(r*1e3,sigma_r(rpm_plot,:)/1e6,'k','linewidth',3)
126 ends = ((max(sigma_r(rpm_plot,:))/1e6) - min(sigma_r(rpm_plot,:))/1e6)/10;
127 axis([r(1)*1e3 r(end)*1e3 min(sigma_r(rpm_plot,:)/1e6)-ends ...
128     max(sigma_r(rpm_plot,:))/1e6+ends])
129 ylabel('\sigma_r [MPa]')
130 xlabel('r [mm]')
131 grid on
132
133 subplot(3,1,2)
134 plot(r*1e3,sigma_t(rpm_plot,:)/1e6,'k','linewidth',3)
135 ends = ((max(sigma_t(rpm_plot,:))/1e6) - min(sigma_t(rpm_plot,:))/1e6)/10;
136 axis([r(1)*1e3 r(end)*1e3 min(sigma_t(rpm_plot,:)/1e6)-ends ...
137     max(sigma_t(rpm_plot,:))/1e6+ends])
138 ylabel('\sigma_t [MPa]')
```

(continues)

Appendix 2. (continued)

```
xlabel('r [mm]')
grid on

subplot(3,1,3)
plot(r*1e3,sigma_von_mises(rpm_plot,:)/1e6,'k','linewidth',3)
ends = ((max(sigma_von_mises(rpm_plot,:))/1e6) - ...
    min(sigma_von_mises(rpm_plot,:))/1e6)/20;
axis([r(1)*1e3 r(end)*1e3 min(sigma_von_mises(rpm_plot,:)/1e6)-ends ...
    max(sigma_von_mises(rpm_plot,:))/1e6+ends])
ylabel('\sigma_v_o_n_M_i_s_e_s [MPa]')
xlabel('r [mm]')
grid on
```

Appendix 3. Figures of fabricated Configuration I test rig

Figure A3.1. Fabricated rotor

(continues)

Appendix 3. (continued)

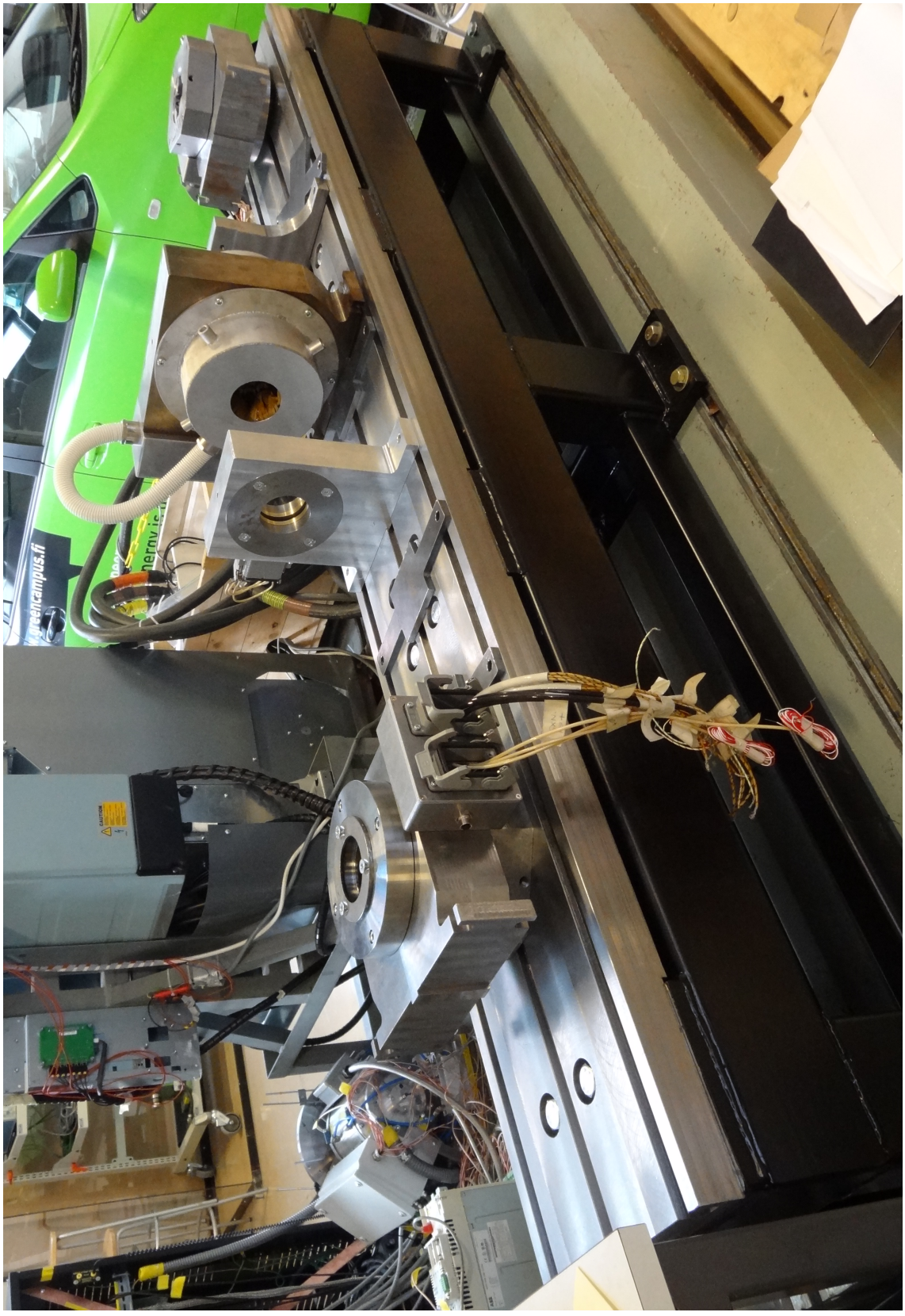

Figure A3.2. Fabricated base plate and supporting structure with actuator modules